1
2
Diverse characteristics of extreme orographic snowfall events in Little Cottonwood Canyon, Utah

3
Michael L. Wasserstein[a] and W. James Steenburgh[a]

4
[a] *Department of Atmospheric Sciences, University of Utah, Salt Lake City, UT*

5

6
Corresponding author: Michael L. Wasserstein, michael.wasserstein@utah.edu

ABSTRACT

7

8   Heavy orographic snowfall can disrupt transportation and threaten life and property in

9   mountainous regions but benefits water resources, winter sports, and tourism. Little

10 Cottonwood Canyon (LCC) in northern Utah's Wasatch Range is one of the snowiest

11 locations in the interior western United States and frequently observes orographic snowfall

12 extremes with threats to transportation, structures, and public safety due to storm-related

13 avalanche hazards. Using manual new-snow and liquid precipitation equivalent (LPE)

14 observations, ERA5 reanalyses, and operational radar data, this paper examines the

15 characteristics of cool-season (October–April) 12-h snowfall extremes in upper LCC. The 12-

16 h extremes, defined based on either 95th percentile new snow or LPE, occur for a wide range

17 of crest-level flow directions. The distribution of LPE extremes is bimodal with maxima for

18 south-southwest or north-northwest flow whereas new snow extremes occur most frequently

19 during west-northwest flow, which features colder storms with higher snow-to-liquid ratios.

20 Both snowfall and LPE extremes are produced by diverse synoptic patterns, including inland-

21 penetrating or decaying atmospheric rivers from the south through northwest that avoid the

22 southern high Sierra Nevada, frontal systems, post-cold-frontal northwesterly flow, south-

23 southwesterly cold-core flow, and closed low pressure systems. Although often associated

24 with heavy precipitation in other mountainous regions, the linkages between local integrated

25 water vapor transport (IVT) and orographic precipitation extremes in LCC are relatively

26 weak, and during post-cold-frontal northwesterly flow, highly localized and intense snowfall

27 can occur despite low IVT. These results illustrate the remarkable diversity of storm

28 characteristics producing orographic snowfall extremes at this interior continental mountain

29 location.

SIGNIFICANCE STATEMENT

30

31   Little Cottonwood Canyon in northern Utah's central Wasatch Range frequently

32 experiences extreme snowfall events that pose threats to life and property. In this study we

33 illustrate the large diversity of storm characteristics that produce this extreme snowfall.

34 Meteorologists commonly use the amount of water vapor transport in the atmosphere to

35 predict heavy mountain precipitation, but that metric has limited utility in Little Cottonwood

36 Canyon where heavy snowfall can occur with lower values of such transport. Our results can

37 aid weather forecasting in the central Wasatch Range and have implications for

38 understanding precipitation processes in mountain ranges throughout the world.

1. Introduction

Orographic precipitation extremes in the form of heavy rainfall, snowfall, or other forms of precipitation can produce wide-ranging geophysical hazards and societal impacts including flooding (Maddox et al. 1978; Ralph et al. 2006; Neiman et al. 2011; Froidevaux and Martius 2016), avalanches (Schweizer et al. 2003, 2009; Farestveit and Skutlaberg 2009; Conlan and Jamieson 2016a,b), landslides (Johnston et al. 2021), structural collapses (Hilker et al. 2009), power outages (Roebber and Gyakum 2003), and immobilized transportation (Nöthiger and Elsasser 2004). Such extremes occur frequently during moist flow over hills and mountains with orographic lift enhancing precipitation rates through processes that include seeder-feeder and potential instability release (Roe 2005; Houze 2012; Colle et al. 2013; Stoelinga et al. 2013). Orographic precipitation extremes have been linked to atmospheric rivers (Neiman et al. 2011; Lavers and Villarini 2013; Froidevaux and Martius 2016; Lorente-Plazas et al. 2018), convective storms (Caracena et al. 1979; Wulfmeyer et al. 2011; Casaretto et al. 2022), lake- and sea-effect precipitation (Manabe 1957; Campbell et al. 2018; Veals et al. 2020; Steenburgh and Nakai 2020), extratropical cyclones (Lackmann and Gyakum 1999; Pandey et al. 1999; Viale and Nuñez 2011), and tropical cyclones (Smith et al. 2009; DeHart and Houze 2017), including those undergoing extratropical transition (Sinclair 1993; Sturdevant-Rees et al. 2001; Stohl et al. 2008; Liu and Smith 2016; Lentink et al. 2018). Often, the intensity and spatial distribution of orographic precipitation is closely related to the wind (or vapor transport) direction, with precipitation heaviest along or upstream of ridgelines that are aligned orthogonal to the flow (Houze et al. 2001; James and Houze 2005; Yuter et al. 2011; Foresti et al. 2018). For many regions — such as North America's Cascade Range, Olympic Mountains, and Sierra Nevada, or the European Alps — distinct synoptic patterns directly influence the location of extreme orographic precipitation (e.g. Pandey et al. 1999; Minder et al. 2008; Yuter et al. 2011; Froidevaux and Martius 2016); in contrast, *several* different synoptic types can produce orographic precipitation extremes in some regions like Italy's Apennine Range (e.g. Capozzi et al. 2022).

Cool-season orographic snowfall extremes occur frequently in the Wasatch Range of northern Utah, a narrow, quasi-meridionally oriented mountain range at the eastern periphery of the Great Basin in the interior western United States (Fig. 1a,b). The Wasatch Range broadens east of the Salt Lake Valley where a series of zonally oriented ridges (Alpine, Cottonwood, and Wildcat) and canyons [Little Cottonwood (LCC), Big Cottonwood (BCC), and Mill Creek (MCC)] compose a significant portion of what is known locally as the central
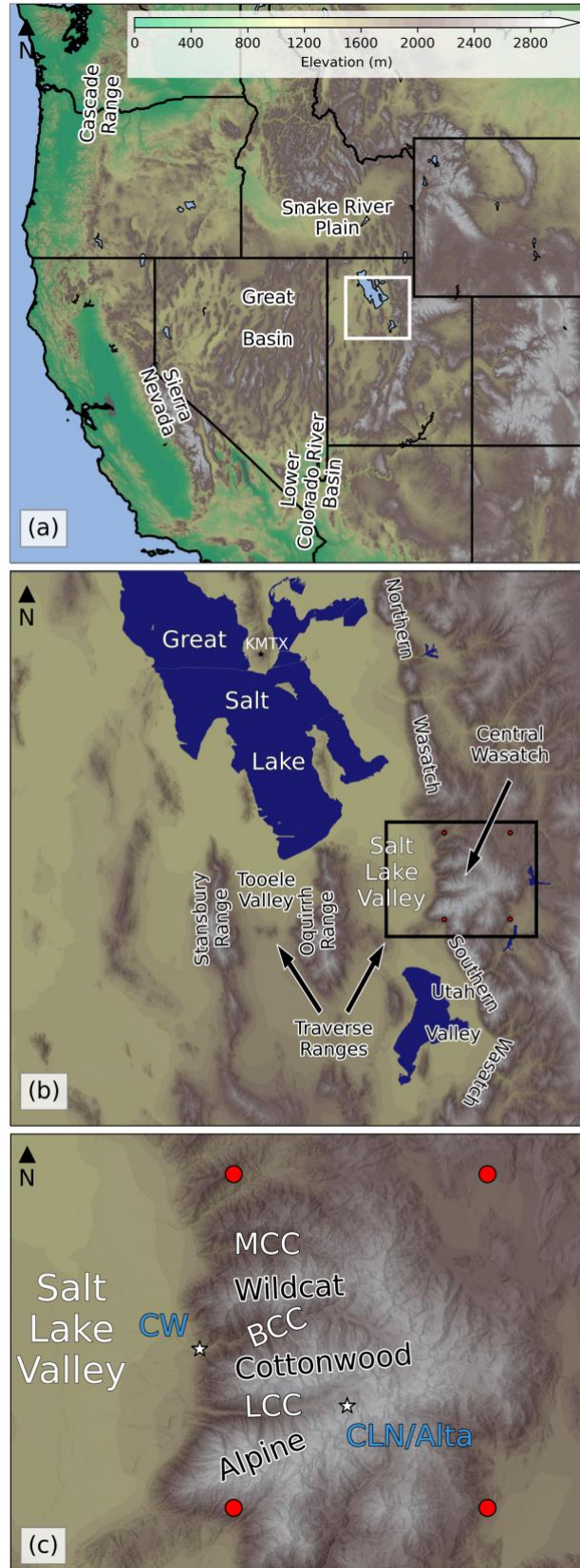
Figure 1. Topography of (a) the western United States (scale at top), (b) the central Wasatch and surrounding region [identified by white box in (a)], and (c) the central Wasatch [identified black by box in (b)] with key geographic features annotated and four ERA5 grid points used to determine meteorological characteristics identified by red dots.

73   Wasatch Range (hereafter central Wasatch; Fig. 1c). Little Cottonwood Canyon splits the

74   Alpine and Cottonwood ridges, which rise to ~3300 m MSL, more than 2000 m above the

75   Salt Lake Valley and Great Salt Lake (GSL). Mean cool-season (October–April) snowfall

76   and liquid precipitation equivalent (LPE) [both based on daily NWS Cooperative Observer

77   Program (COOP) station reports] increase from 207 cm and 432 mm at Cottonwood Weir

78   (CW; see Fig. 1c; 1520 m MSL) at the western base of the central Wasatch to 1106 cm and

79   902 mm at Alta (2655 m MSL) in upper LCC (NCEI 2021). The snowfall and LPE increase

80   with elevation reflect orographic enhancement, with the snowfall increase also affected by a

81   greater fraction of precipitation falling as snow at upper elevations, which is near 100% at

82   and above 2600 m MSL (Steenburgh 2023).

83   Within LCC, a two-lane highway, State Route 210 (SR-210), is the only transportation

84   link to Alta. The road climbs 1000 m in 13 km, crossing 50 avalanche paths that leave it

85   vulnerable to avalanches during frequent cool-season storms (Steenburgh 2023). Due to

86   heavy traffic volumes, a lack of avalanche defense structures, and the large concentration of

87   avalanche paths, SR-210 has the highest uncontrolled avalanche hazard index of any major

88   road in the world (Schaerer 1989; Nalli and Mckee 2018). During and after periods of heavy

89   snowfall, which is the strongest forecasting parameter for large new-snow avalanches (e.g.,

90   Föhn et al. 2002; Schweizer et al. 2003), dangerous avalanche conditions can force the

91   closure of the SR-210, threaten lives and property in the Town of Alta and nearby Village of

92   Snowbird, and induce travel restrictions known as interlodge during which residents and

93   visitors are legally mandated to remain indoors (Steenburgh 2023); during a particularly

94   intense storm in February 2020, interlodge lasted for 52 consecutive hours. During the

95   2022/23 cool season, extreme snowfall and avalanches forced frequent multiday closures of

96   SR-210, stranding residents and visitors and leading to food shortages (Jag 2023). The

97   estimated revenue loss for ski areas and other businesses in upper LCC during the closure of

98   SR-210 was \$1.4 million day^{-1} in the 1991/92 season (Blattenberger and Fowles 1995), or

99   about \$3 million day^{-1} in 2023 dollars.

100   Snowfall in the central Wasatch can be produced by 1) unstable, post-cold-frontal

101   northwesterly flow, 2) cold-frontal passages, 3) decaying or inland-penetrating atmospheric

102   rivers 4) localized lake-effect convection, and 5) closed upper-level low pressure systems

103   (Dunn 1983; Carpenter 1993; Horel and Gibson 1994; Steenburgh 2003; Rutz and

104   Steenburgh 2012; Alcott et al. 2012; Rutz et al. 2015). Dunn (1983) identified a maximum in

105   the frequency of high LPE snowfall events at Alta with west-northwest flow (~290°), with

106   the heaviest events produced by northwest flow (310–320°). He speculated that this was due

5

to low-level convergence coupled with orographic lift and lake-effect storms. Northern Utah features a local maximum in strong cold-frontal passage frequency in the Intermountain West, as delineated by an abrupt temperature fall and pressure rise (Shafer and Steenburgh 2008). In some Wasatch storms, cold-frontal passages can feature an intrusion of low-θ_e air aloft, enabling heavy convective precipitation in the pre-frontal phase (Steenburgh 2003). Cold-frontal passages can also be accompanied by heavy precipitation and be followed by post-frontal orographic and GSL-effect precipitation (Steenburgh 2003). Though it only represents about 5% of the total cool-season LPE in the central Wasatch, the GSL-effect can produce heavy snowfall, especially in the early and latter parts of the cool season (Carpenter 1993; Steenburgh et al. 2000; Alcott et al. 2012; Alcott and Steenburgh 2013; Yeager et al. 2013). Prior research has linked inland penetrating or decaying atmospheric rivers from the Pacific Ocean with orographic precipitation in the Wasatch, although they have not been examined systematically (Dettinger et al. 2011; Rutz and Steenburgh 2012; Rutz et al. 2014, 2015). Intermountain cyclones have also been tied to snowfall in the Wasatch (Zishka and Smith 1980; Whittaker and Horn 1981; Dunn 1983; Horel and Gibson 1994), often causing a decreased ratio of mountain to valley LPE (Williams and Peck 1962; Dunn 1983).

Although previous research has examined individual phenomena that contribute to extreme orographic snowfall in LCC, no studies have comprehensively analyzed the orographic snowfall characteristics and associated synoptic regimes. In this paper, we aim to fill this gap using modern reanalyses and radar observations. Additionally, most prior research on orographic precipitation has focused on extreme snowfall in the form of LPE, and as we will show here, the characteristics of extreme snow events differ somewhat from extreme LPE snowfall events since the former is also affected by the snow-to-liquid ratio (SLR). In section 2, we describe the data and methods used. In section 3, we present the seasonal and event characteristics of snowfall at a high-elevation observing site in upper LCC and discuss the flow dependencies, vapor-transport tendencies, synoptic environments, and radar characteristics associated with extreme snowfall events. Section 4 summarizes our results, which will aid forecasting, avalanche hazard assessment, and road-weather maintenance in Little Cottonwood Canyon and enhance knowledge of the mechanisms contributing to orographic precipitation extremes in mountainous regions.

2. Data and Methods

a. Alta-Collins (CLN) snowfall observations

139   We used 12-h manual snow and LPE observations collected by the Alta Ski Patrol at their

140   Alta-Collins (CLN) snow-study plot (2945 m MSL; see Fig. 1 for location) from the 2000–

141   2022 cool seasons (year defined by the ending calendar year) to develop long-term statistics

142   and identify snowfall extremes (Wasserstein and Steenburgh 2023). In the present climate,

143   virtually all the cool-season precipitation at this altitude falls as snow. *Therefore, for the*

144   *purposes of this analysis, "snow" represents the measured 12-h new-snow depth, "LPE" the*

145   *water equivalent of that snow, and "snowfall" precipitation falling in the form of snow*. The

146   snow and LPE measurements were collected in a forested clearing on a standard snowboard

147   placed on the existing snowpack at 0400 and 1600 LST, with LPE obtained with a

148   Snowmetrics sampling tube and scale since at least 2002 (prior sampling method unknown).

149   Alcott and Steenburgh (2010) used 24-h measurements from this location to examine snow-

150   to-liquid ratio at Alta, but we use 12-h observations here since the higher-frequency

151   measurements are now being provided by Alta Ski Patrol and there is less evolution in the

152   synoptic conditions during the shorter period. Although recorded in inches and hundredths of

153   an inch, throughout this paper, we use units of cm and mm for snow and LPE, respectively.

154   We quality controlled the data through comparison with precipitation and snow observations

155   at the nearby Alta National Weather Service COOP site (2655 m MSL) and the Utah

156   Department of Transportation Alta Guard Station (2682 m MSL) and by examining synoptic

157   reanalyses during precipitation periods. There were 4 measurements that we deemed

158   questionable, and we either adjusted the date and time to match nearby observations and

159   reanalysis data or eliminated the observation entirely (Table 1). Each questionable event

160   occurred in October, before Alta Ski Area opened for the season, which may have contributed

161   to a mislabeling of an observation date or measurement.

Table 1. Adjustments made to CLN snow and LPE observations.

Original Event End Time (LST)	New Event End Time (LST)
0400 17 Oct 2004	Removed from analysis
0400 23 Oct 2004	0400 24 Oct 2004
1600 30 Oct 2004	1600 31 Oct 2004
0400 27 Oct 2010	1600 27 Oct 2010

162   We defined 12-h periods with ≥ 2.54 cm of snow as a "snow event" and ≥ 2.54 mm of

163   LPE as an "LPE event". These thresholds eliminate the lowest snow and LPE observations in

164   the dataset, with the former being the minimum recorded snowfall amount for a majority of

165   the observational period (i.e., since 2002) and reliable manual measurement of the latter

166   being difficult when snowfall or LPE are low. We identified the 95th percentile of snow or

167   LPE during these events and classified each as a "snow extreme" or an "LPE extreme." Thus,

168   these are 12-h extremes rather than 24-h or multiday events. Tables A1 and A2 in the online

169   supplemental material list the dates of each snow and LPE extreme and important variables

170   for this study associated with each extreme. Although 26 (19%) of the snow and 30 (26%) of

171   the LPE extremes occurred during consecutive 12-h periods that last either 24 or 36 hours, we

172   treat each as its own event in this paper since removing all but one 12-h period in each of the

173   consecutive periods did not change the results.

174   *b. ERA5 reanalysis*

175   To examine the meteorological conditions associated with orographic snowfall at CLN,

176   we used the European Centre for Medium-Range Weather Forecasts Reanalysis v5 (ERA5;

177   Hersbach et al. 2020). The ERA5 contains global meteorological variables on a 0.25° grid at

178   hourly intervals on pressure levels ranging from 1000 hPa to 1 hPa. There are four ERA5 grid

179   points that surround the central Wasatch (see Fig. 1 for locations), and we averaged data over

180   those four grid points to classify the local meteorological conditions at the mid-point of each

181   12-h observation period. Sensitivity testing revealed that using the start time, end time, or

182   time average for the 12-h period did not substantially impact results. We binned all events

183   into 1 of 16 wind directions (e.g., north, north-northeast, northeast, etc.) using the 700-hPa

184   (the closest mandatory pressure level to crest level) wind direction.

185   *c. KMTX radar*

186   To examine the characteristics of mesoscale precipitation features during orographic

187   snowfall extremes at CLN, we used level II data (NOAA 1991) from the Salt Lake City

188   (KMTX) WSR-88D radar located at 2000 m MSL on Promontory Point above the Great Salt

189   Lake (Fig. 1b). We focus on events beginning with the 2009 cool season when the resolution

190   of the radar data increased to super-resolution. For LPE extremes, none of the 75 events that

191   occurred during or after the 2009 cool season had missing radar data, and for snow extremes,

192   data were missing for only one of the 83 events (1.2%). To study the spatial distribution of

193   precipitation, we examined the frequency of radar echoes ≥ 10 dBZ for all available 0.5°

8

194   radar scans during events. We used 10 dBZ because it represents an approximate threshold

195   for accumulating snowfall and has been used in prior studies in northern Utah (e.g.,

196   Steenburgh et al. 2000; Yeager et al. 2013). KMTX often experiences beam blockage by the

197   Wasatch Range and the 0.5° scan can overshoot or undesample shallow orographic

198   convection, reducing the accuracy of quantitative precipitation estimates at specific locations

199   (Wood et al. 2003). Thus, we use a fixed dBZ threshold, rather than an LPE estimate, to

200   characterize the spatial precipitation patterns associated with snowfall.

201   *d. Synoptic Classficiations*

202   We manually classified all snow and LPE extremes into 1 of 8 synoptic classifications

203   that we identified using ERA5 analyses of 500-hPa geopotential height and absolute vorticity,

204   sea level pressure, 700-hPa temperature, 700-hPa relative humidity, 700-hPa wind, and

205   vertically integrated water vapor transport (IVT) magnitude and vectors at the mid-point of

206   each event. Radar imagery was sometimes consulted to ascertain the nature of precipitation

207   features (e.g., frontal, post-frontal convection, etc.). We calculated IVT from the ERA5

208   surface to 300-hPa using

$$ \text{IVT} = \sqrt{\left(\frac{1}{g}\int_{sfc}^{300} qu\ dp\right)^2 + \left(\frac{1}{g}\int_{sfc}^{300} qv\ dp\right)^2}, \tag{1} $$

209   where q is specific humidity in kg kg^{-1}, u and v are the zonal and meridional winds in m s^{-1},

210   p is pressure in Pa, and g is the acceleration due to gravity. We used 8 synoptic

211   classifications: southerly IVT (SIVT), southwesterly IVT (SWIVT), westerly IVT (WIVT),

212   northwesterly IVT (NWIVT), post-cold-frontal northwesterly flow (NW Postfrontal), cold-

213   fronts or baroclinic troughs (Frontal), south-southwesterly cold core flow (SW Cold Core)

214   and closed low pressure systems (Closed Low). The IVT events were associated with

215   elevated IVT, typically extending toward the central Wasatch from the classification

216   direction, with mean IVT over the central Wasatch $\geq$ 100 kg m^{-1} s^{-1}. These events featured

217   elongated corridors of elevated IVT, but magnitudes over the central Wasatch may be below

218   the commonly used threshold for an atmospheric river (250 kg m^{-1} s^{-1}) due to declining IVT

219   with inland penetration (Rutz et al. 2014, 2015). The classification direction was based on the

220   ERA5 700-hPa wind direction (i.e., 157.5-202.5°, 202.5-247.5°, 247.5-292.5°, and 292.5-

221   332.5° for the SIVT, SWIVT, WIVT, and NWIVT events, respectively), which approximates

File generated with AMS Word template 2.0

222 the crest-level water vapor transport direction and is often used by local forecasters to

223 anticipate local orographic precipitation enhancement. Results based on IVT direction were

224 comparable. Two events with a weak short-wave trough embedded in large-scale westerly

225 flow fell in the SWIVT classification based on these objective criteria. We modified these

226 events to WIVT as that was the predominate large-scale flow direction. The NW Postfrontal

227 events featured northwesterly 700-hPa flow in the wake of a 700-hPa front or trough with the

228 central Wasatch experiencing cold or weak advection. Frontal events were associated with a

229 cold front, quasi-stationary front, or baroclinic trough and associated precipitation band.

230 Some Frontal events had mean IVT over the central Wasatch ≥ 100 kg m^{-1} s^{-1}, meeting the

231 minimum criteria for classification as an IVT event, but their frontal characteristics

232 distinguish them from events in the IVT classifications. The SW Cold Core events were

233 produced by a deep upper-level trough over the southwest US with the central Wasatch in

234 cold core south-southwesterly flow. These events also featured lower IVT (i.e., < 100 kg m^{-1}

235 s^{-1}). Lastly, events with closed 700-hPa circulation near or over northern Utah with the

236 central Wasatch in the frontal baroclinity or thermal warm tongue just ahead of the low center

237 fell in the Closed Low classification. We labeled events that did not clearly fit in any one of

238 those 8 classifications as not applicable (N.A.). These events could have featured: (1) IVT $<$

239 100 kg m^{-1} s^{-1}, failing to meet the criteria for an IVT event, (2) elements of multiple

240 classifications, (3) synoptic frontal characteristics (e.g., wind shift and baroclinity) but either

241 radar data was not available to confirm the presence of a frontal precipitation band or such a

242 band wasn't evident in radar, or (4) characteristics that did not fit any of the eight categories.

3. Results

a. Event and seasonal snowfall characteristics

245   We begin with an examination of event, monthly, and seasonal snow and LPE

246 characteristics at CLN in upper LCC. We identified 2707 snow events over the 23-year

247 period, with a mean and median of 11.2 cm and 7.6 cm, respectively (Fig. 2a). As is often the

248 case with precipitation (e.g., Martinez-Villalobos and Neelin 2019), the event-size frequency

249 exhibited a gamma distribution with over 1700 events < 12.5 cm, $10 \geq 48.5$ cm, and a

250 maximum of 64.8 cm. There were 138 95th percentile snow extremes with ≥ 30.5 cm of snow.
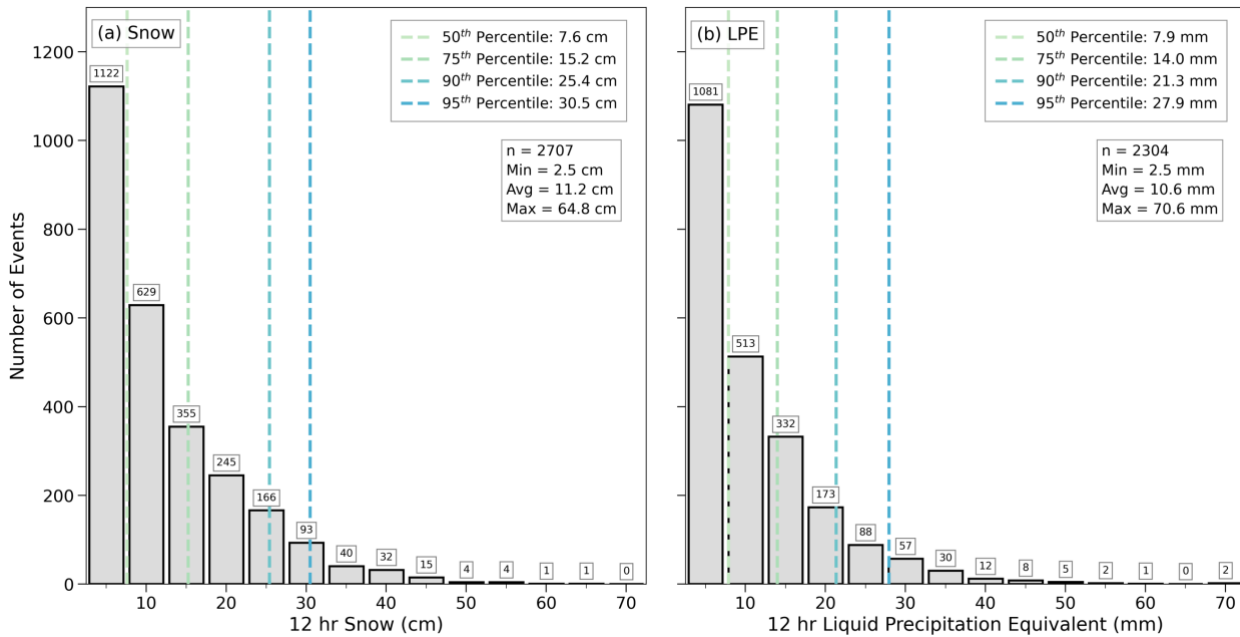
Figure 2. Histograms of 12-hr (a) snow and (b) LPE events at CLN during the 2000–2022 cool seasons. Bins in (a) are in 5-cm increments starting at 2.5 cm and (b) are in 5-mm increments starting at 2.5 mm. Dashed vertical lines indicate the 50th, 75th, 90th, and 95th percentiles. Number of events in each bin annotated at top of bar.

251   For LPE, we identified 2304 events with a mean and median of 10.6 mm and 7.9 mm,

252   respectively (Fig. 2b). The event-size distribution was similar to snow with an abundance of

253   small events, $10 \geq 48.5$ mm, and a maximum of 70.6 mm. There were 116 95th percentile

254   LPE extremes with ≥ 27.9 mm of LPE. Only 52 events met *both* the extreme snow and LPE

255   thresholds.

256   Featuring a transitional (a.k.a. intermountain) snow climate, the central Wasatch observes

257   high seasonal snow and moderate wintertime temperatures with elements of continental or

258   coastal snow climates depending on the season (Whiteman 2000; Mock and Birkeland 2000).

259   During the 23-season study period, seasonal snow at CLN ranged from 831.9–1877.1 cm and

260   LPE ranged from 726.4–1681.7 mm, with means of 1340.4 cm and 1116.9 mm, respectively

261   (Fig. 3). The 2011 cool season produced the most snow (181) and LPE (196) events, whereas

262   the 2015 cool season saw the fewest snow (96) and LPE (109) events. Median monthly snow

263   and LPE increased from October to December, consistent with the transition to the cool

264   season (Fig. 4). Median monthly snow and LPE from December to April are ~200 cm and

265   ~175 mm, respectively, and, although there are variations from month to month, the

266   differences are not statistically significant at the 95th percent confidence interval (hereafter,

267   statements of significance are based on a 95th percent confidence interval).
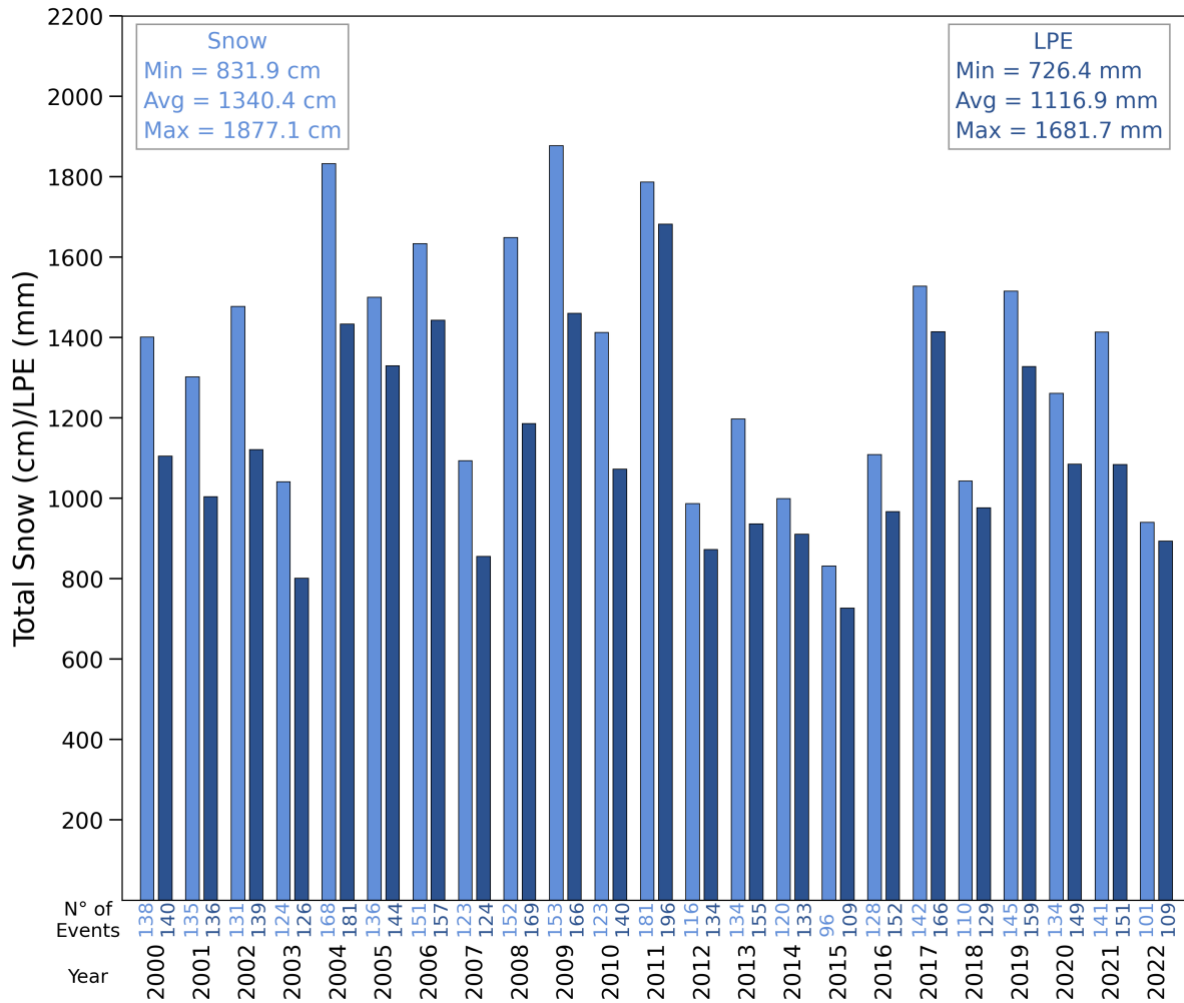
File generated with AMS Word template 2.0

Figure 3. Total seasonal snow (cm, light blue) and LPE (mm, dark blue) during the 2000–2022 cool seasons. Number of events during each season annotated at bottom of bars.

268   Indicative of the large variety of storm tracks and types that produce orographic snowfall

269   extremes in the central Wasatch, there is a wide range of snow-to-liquid ratios (SLR) in

270   individual 12-h periods at CLN. We generated SLR statistics for the 1903 events with ≥ 5.1

271   cm of snow and ≥ 2.8 mm of LPE in the 23-season study period. These criteria reduce

272   relative errors in SLR due to rounding and measurement (Judson and Doesken 2000; Roebber

273   et al. 2003; Baxter et al. 2005). Snow-to-liquid ratio in these periods ranged from 1.6 to 50,

274   with a mean of 13.8 and a median of 12.8 (Fig. 5), comparable to results from Alcott and

275   Steenburgh (2013), who found a mean of 14.4 and a median of 13.3 at CLN for Nov–Apr

276   1999–2007. Our lower values are likely due to our inclusion of October in our analysis and

277   the different study period that includes observations through 2022.
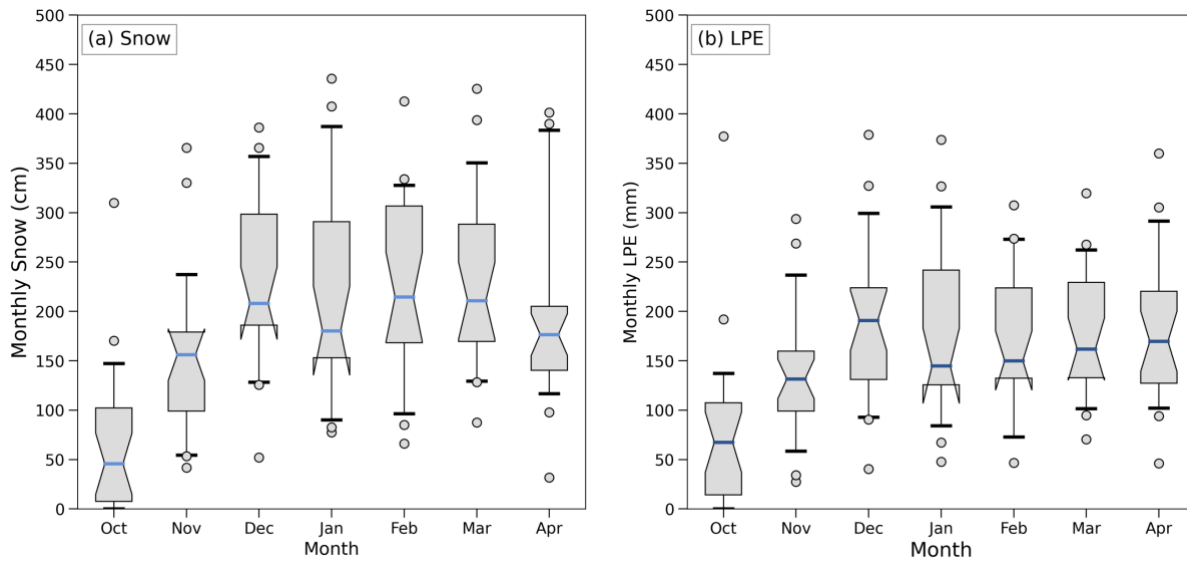
File generated with AMS Word template 2.0

Figure 4. Box-and-whisker plots of monthly (a) snow and (b) LPE at CLN during the 2000–2022 cool seasons. The colored horizontal line represents the median, the box the 25th to 75th percentile, the whiskers the 5th and 95th percentiles, and the circles outliers. Notches indicate the 95 percent confidence interval of the median as computed using Gaussian-based asymptotic approximation.

278   The El Niño Southern Oscillation (ENSO) is an important driver of weather and climate

279   variability in the continental western United States (Bjerknes 1966, 1969; Rowntree 1972;

280   Horel and Wallace 1981; Ropelewski and Halpert 1986; Trenberth et al. 1998). Although

281   ENSO phase can have seasonal precipitation impacts on regions in the American west [e.g.

282   positive ENSO has links to increased precipitation in California (Cayan et al. 1999; Jong et

283   al. 2016), and negative ENSO has links to increased precipitation in the Pacific Northwest

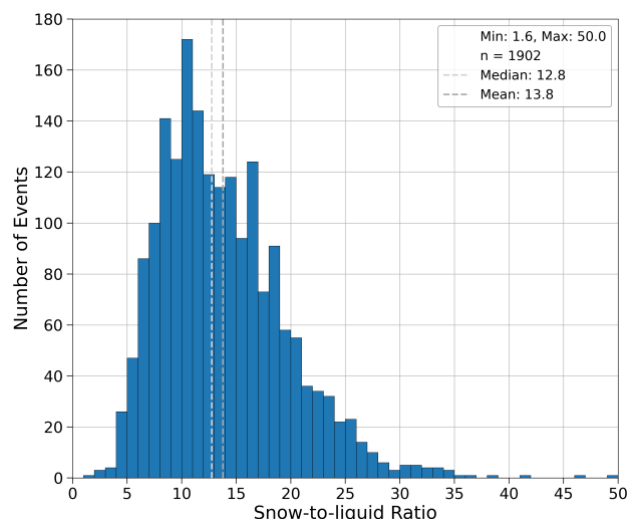284   (Redmond and Koch 1991)], northern Utah's mountains fall at the nodal point in the ENSO

Figure 5. Histogram of snow-to-liquid ratio for all events at CLN with ≥ 5.1 cm of snow and ≥ 2.8 mm of LPE. Bins have a width of 1. Light and dark grey lines indicate the median and mean, respectively.
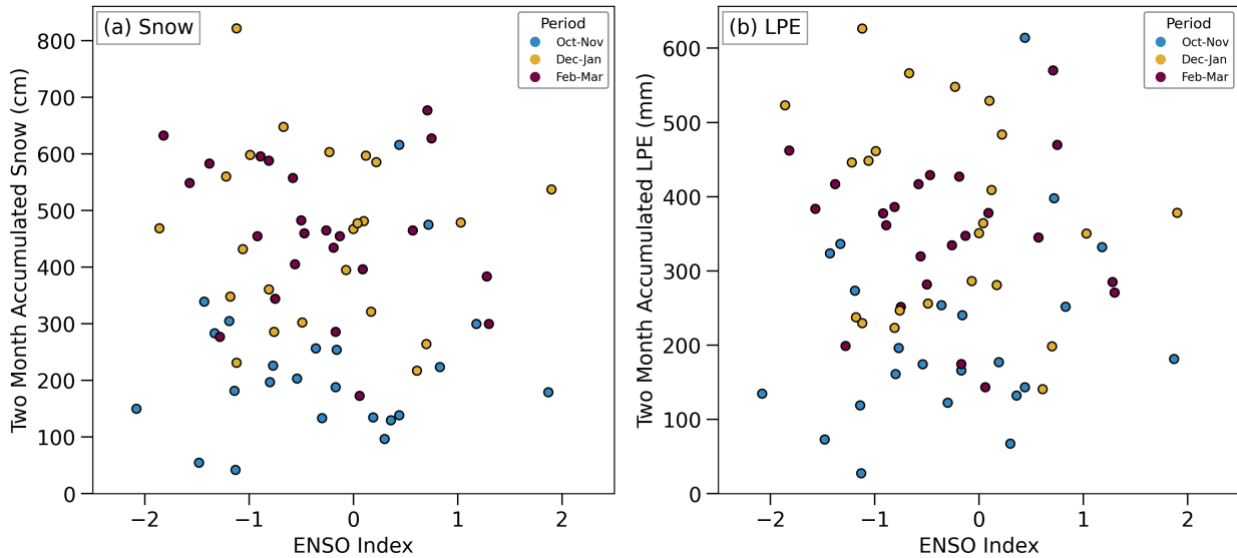
Figure 6. Scatter plot of ENSO index and (a) two-month accumulated snow and (b) two-month accumulated LPE at CLN.

285   dipole where ENSO phase has little correlation with seasonal precipitation trends (Redmond

286   and Koch 1991). Using snow and LPE data at CLN and the multivariate ENSO index version

287   2 (MEI.v2; available at https://psl.noaa.gov/enso/mei; Wolter and Timlin 2011), we analyzed

288   the relationship between ENSO index and two-month accumulated snow (Fig. 6a) and LPE

289   (Fig. 6b). Consistent with prior research, ENSO has no discernable relationship with

290   observed snow or LPE at CLN. In any two-month sub-seasonal period, strong positive ENSO

291   periods (i.e. ENSO index $\geq$ 1.5) and strong negative ENSO periods (i.e. ENSO index $\leq$ -1.5)

292   do not consistently produce more or less snow or LPE at CLN than neutral phases or weak

293   periods. The Pearson correlation coefficients between two-month ENSO index and snow and

294   LPE were -0.03 and -0.01, respectively, indicative of the lack of relationship between ENSO

295   and snowfall in the central Wasatch.

296   *b. Flow dependencies*

297   We now examine the relationship between the 700-hPa (near crest level) flow and

298   orographic snowfall extremes at CLN. For context, the cool-season climatological 700-hPa

299   wind directions are most frequently southerly to northwesterly with wind speeds of 5–10

300   m s^{-1} (Fig. 7a). There is weak bimodality in the wind direction frequency with maxima from

301   the west-northwest and south-southwest. Higher wind speeds are also more frequent from

302   these flow directions. A similar distribution exists for all snow and LPE events, although the

303   bimodality strengthens and west-northwesterly flow emerges as the primary maximum (Figs.

304   7b,c). This indicates a greater likelihood of snowfall during west-northwesterly flow than

14

305   other flow directions. For snow extremes, the west-northwesterly flow maximum strengthens

306   further, although such events occur for a wide range of flow directions and there is a weak

307   secondary maximum for west-southwesterly flow (Fig. 7d). To illustrate the primacy of the

308   west-northwesterly flow snow maximum, 80 (58.0%) of the 138 snow extremes featured west

309   to northwest flow and 44 (31.9%) specifically featured from the west-northwest (percentages

310   not shown explicitly in Fig. 7). In contrast, extreme LPE events feature stronger bimodality

311   and a less prominent west-northwesterly flow maximum (Fig. 7e). Additionally, wind speeds

312   are higher for LPE extremes compared to snow extremes.

313   The bimodal relationship of LPE extremes to wind direction contrasts with the modal

314   distributions identified for major precipitation events in the Sierra Nevada (e.g., Pandey et al.

315   1999, see their Fig. 5) and Cascade Range near Portland, Oregon (e.g., Yuter et al. 2011, see

316   their Fig. 2) where the flow interacts with broad, quasi-linear mountain barriers. We

317   hypothesize that the bimodality at CLN reflects three characteristics of the regional terrain

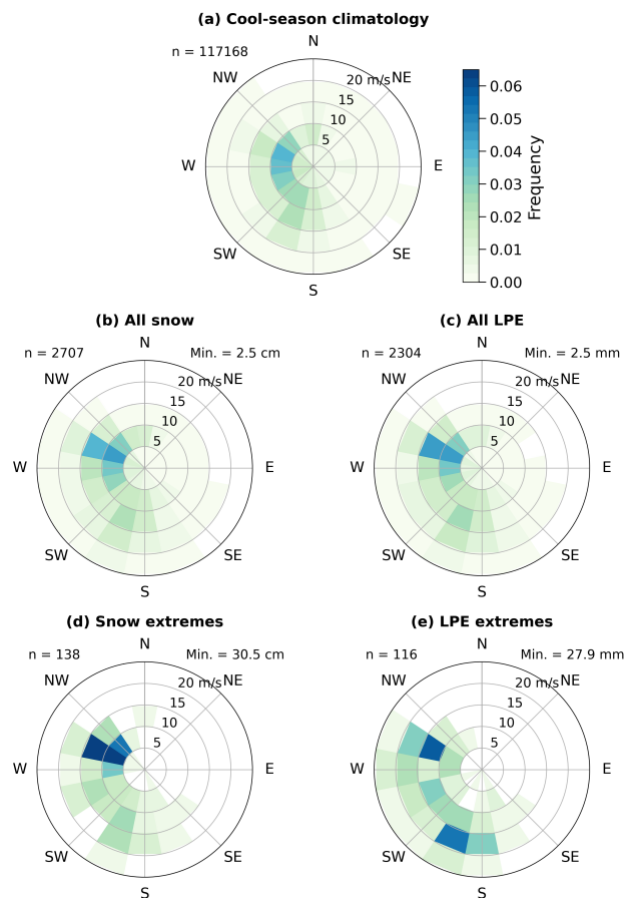318   and geography. The first is the presence of the Oquirrh Range to the west of the central

Figure 7. Normalized polar histograms of 700-hPa wind speed and direction frequency in the central Wasatch. Bins are in 5 m s^{-1} and 22.5° increments. (a) Cool-season climatology. (b-e) As in (a) but for all snow events, all LPE events, snow extremes, and LPE extremes, respectively.

15

File generated with AMS Word template 2.0

319   Wasatch, which lies on a bearing from ~235–290˚ relative to CLN and potentially contributes

320   to a decline in event frequencies in southwest to westerly flow. The Stansbury Range farther

321   upstream could also contribute to this event frequency decline. In addition, during

322   northwesterly flow, blocking by the Oquirrh Range has been shown to enhance convergence

323   and precipitation produced upstream of the central Wasatch over the Salt Lake Valley (Alcott

324   and Steenburgh 2013), potentially contributing to an increase in event frequencies from that

325   flow direction. The second is the broader, three-dimensional topography of the central

326   Wasatch, which includes zonally oriented sub-barrier ridges that are the highest local terrain

327   features and oriented nearly orthogonal to the otherwise quasi-meridional Wasatch Range. As

328   a result, instead of a single optimal flow direction for upslope flow as occurs over a linear

329   barrier, flow from multiple directions is potentially forced over the central Wasatch,

330   especially the high terrain surrounding Little Cottonwood Canyon. The third is the Great Salt

331   Lake, which contributes to lake-effect storms and approximately 5% of the cool-season

332   precipitation in upper Little Cottonwood Canyon during northwesterly flow (Alcott et al.

333   2012; Yeager et al. 2013).

334   The more pronounced west-northwesterly flow maximum for snow extremes compared to

335   LPE extremes reflects the compounding influence of SLR, which exhibits considerable

336   variability at CLN (e.g., Fig. 5) and inversely correlates strongly with the near-crest-level

337   temperature (Alcott and Steenburgh 2010). Thus, while LPE extremes may be favored by

338   higher temperatures when the absolute humidity is higher, snow extremes can occur at lower

339   temperatures when the SLR is large. Indeed, a comparison of the 700-hPa temperatures

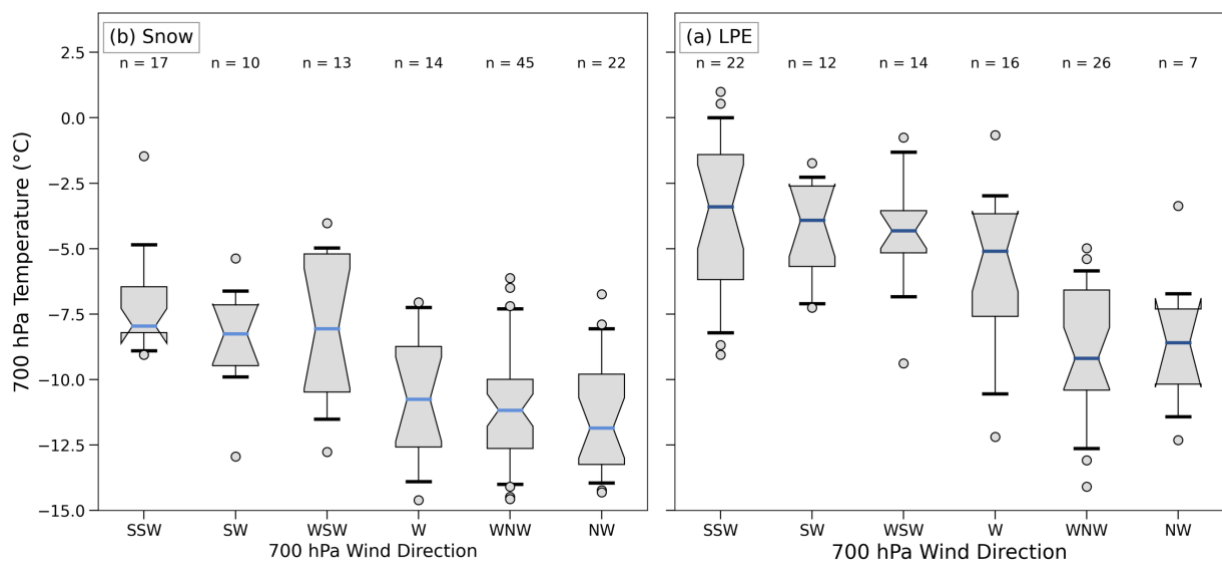340   during snow and LPE extremes shows that the former are substantially colder, with the

Figure 8. Box-and-whisker plots of 700-hPa temperatures for (a) snow and (b) LPE extremes binned by 700-hPa wind direction. Convention same as Fig. 4.

File generated with AMS Word template 2.0

medians 2.0–5.9°C lower depending on the 700-hPa wind direction (cf. Figs. 8a,b). Given the inverse correlation of SLR with near-crest-level temperatures, this leads to substantially higher SLRs in snow extremes compared to LPE extremes (cf. Figs. 9a,b). The pronounced west-northwesterly to northwesterly flow maximum for snow extremes is consistent with such flow directions favoring colder temperatures and higher SLR snowfalls.

An important question concerns the representativeness of the mid-point wind direction in each 12-h period. To examine this, we produced polar histograms of the ERA5 700-hPa wind direction at *each hour* during LPE extremes for each mid-point 700-hPa wind direction (Fig. 12). For brevity, we focus on SSW, SW, WSW, W, WNW, and NW mid-point wind directions because they comprise the bulk of the LPE extremes. Most LPE extremes have little wind direction variability, with the mid-point wind direction being the mode and relatively high frequencies occurring in adjacent direction bins (Fig. 10). Variability, as indicated by a broader wind-direction distribution, was greatest for southwesterly, west-southwesterly, and westerly events, which likely reflects a high frequency of trough passages (Figs. 10b-d). Conversely, events with south-southwesterly, west-northwesterly, and northwesterly flow have greater flow persistence, consistent with a sharper peak at or near those flow directions (Figs. 10a, e, and f). We obtained similar results for snow extremes (not shown).

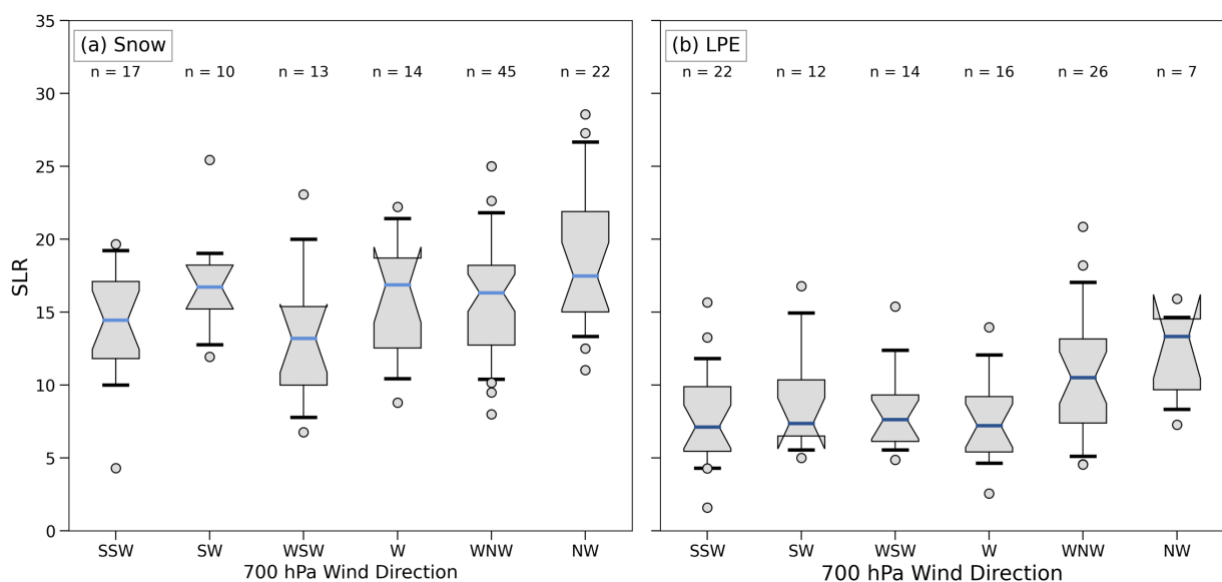Figure 9. As in Fig. 8, but for SLR.

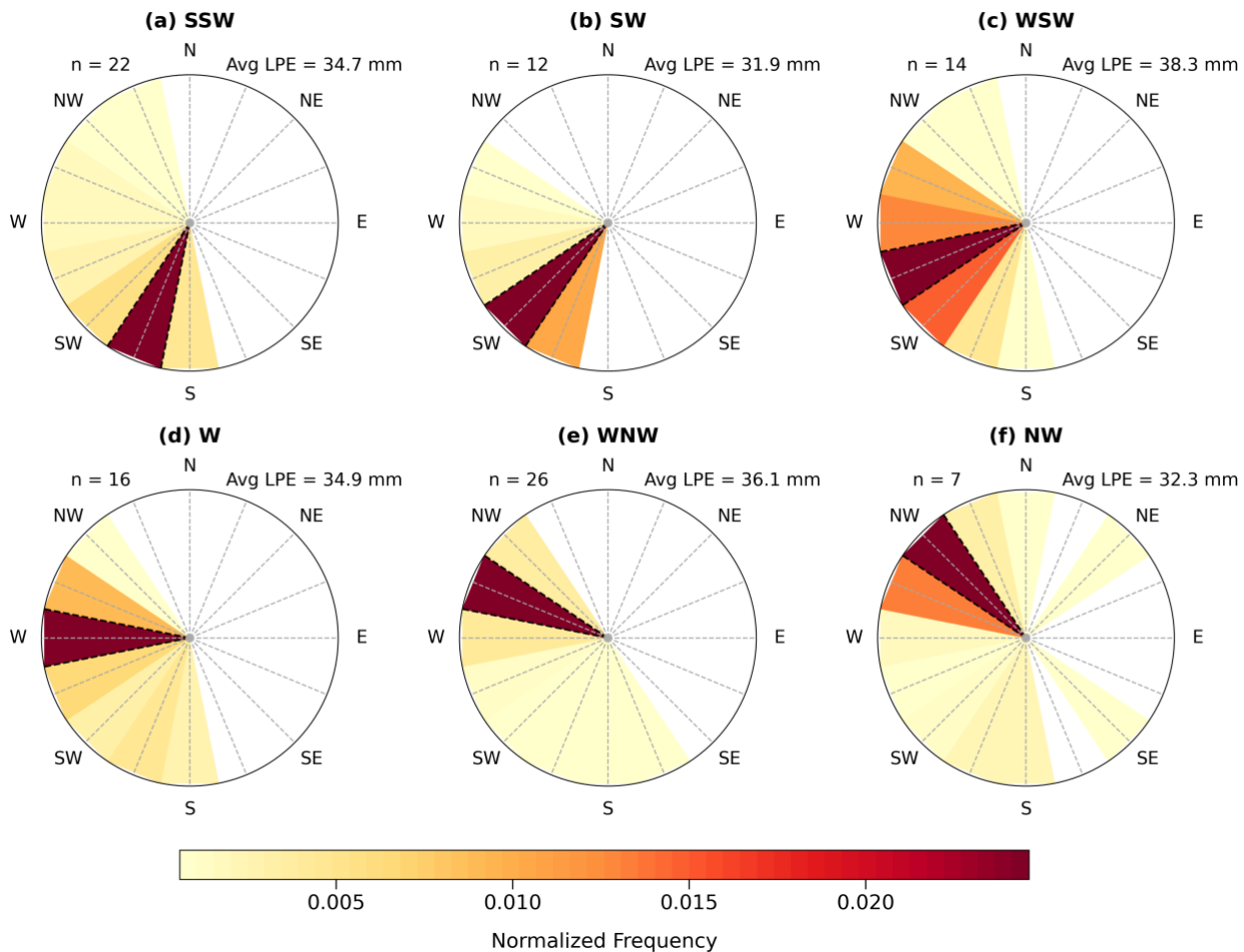File generated with AMS Word template 2.0

Figure 10. Normalized frequency of 700-hPa wind direction during each LPE extreme binned by wind direction classification (color bar at bottom). Number of events listed in the upper left corner. (a) South-southwesterly flow. (b-g) As in (a), but for southwesterly, west-southwesterly, westerly west-northwesterly, and northwesterly flow.

c. Synoptic classifications of extreme events

359   As discussed in section 2d, our manual classification of snow and LPE extremes revealed

360   eight patterns that generate extreme orographic snowfall at CLN (SIVT, SWIVT, WIVT,

361   NWIVT, NW Postfrontal, Frontal, SW Cold Core, and Closed Low). Just under 40% of the

362   LPE extremes fell into one of the high IVT classifications, with SWIVT the most common

363   (Fig. 11). This fraction is much higher than for snow extremes (8%, Fig. 11), likely because

364   high IVT events are often warmer, have lower SLRs, and are less likely to generate snowfall

365   extremes. In contrast, nearly 50% of the snow extremes were NW Postfrontal, compared to

366   only 18% of LPE extremes, which likely reflects the tendency for such events to feature high

367   SLRs and generate large snowfalls from low to moderate LPE. Frontal was the most common

368   LPE classification and the second most common snow classification. For both snow and LPE

369   extremes, SW Cold Core and Closed Low made up less than 10% of events. While these

370   eight synoptic classifications represent the majority of central Wasatch snowstorms, there
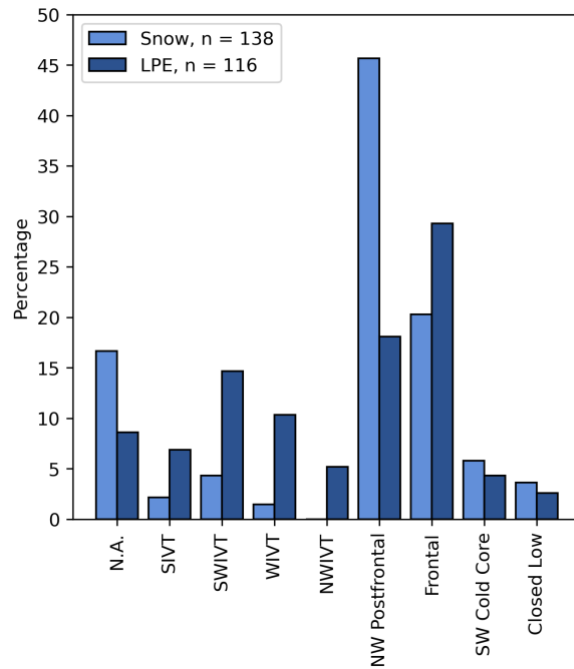
371

Figure 11. Percentage of snow and LPE extremes by synoptic classification.

372   were some snow and LPE extremes which did not fall clearly into any one of the eight

373   synoptic classifications, and we labeled these events as N.A. (Fig. 11).

374   We produced composites of IVT, 500-hPa geopotential height, and 700-hPa temperature

375   and winds for each synoptic type for both snow and LPE extremes. For brevity, we show only

376   the latter since the snow extreme composites were qualitatively similar. Because there were

377   only three LPE extremes that we classified as Closed Low, we omitted Closed Low events

378   from this composite analysis. For each high IVT synoptic type, IVT penetration into the

379   interior occurs to the north or south of the high Sierra Nevada south of Lake Tahoe (Fig. 12a-

380   d; hereafter high Sierra). For the SIVT and SWIVT composites, the high IVT values

381   circumscribe the southern high Sierra and penetrate into northern Utah via the lower

382   Colorado River Basin (Fig. 12a-b). For the WIVT composite, high IVT values extend across

383   the northern Sierra and southern Cascades to northern Utah (Fig. 12c). These results are

384   consistent with Rutz et al. (2014, 2015) who showed that the high Sierra south of Lake Tahoe

385   contribute strongly to declining IVT and AR decay due to water vapor depletion by

386   orographic precipitation. Finally, for the NWIVT composite, the high IVT values move

387   across the Cascade Range and then over the low-elevation Snake River Plain to northern Utah

388   (Fig. 12d). In each high IVT composite, 700-hPa winds over the central Wasatch are ~15 m

389   s^{-1}, stronger than the modal wind speeds at this level which are 5–10 m s^{-1} (see Fig. 7a).

390   Composite 700-hPa temperatures in the central Wasatch are near -3 °C for SIVT, SWIVT,

391   and WIVT and -5 °C for the NWIVT composite (Fig. 12a-d). These are relatively high

392   temperatures for cool-season storms at CLN (see Fig. 8). The strong flow and high

393   temperatures in these high IVT events often result in high LPE but modest snowfall totals.

394   For each composite, the mean SLR is less than 9, substantially less than the mean SLR at

395   CLN of 13.8 (Fig. 5), but comparable with typical SLR values during LPE extremes (Fig.

396   9b).

397   Although over a third of the LPE extremes fall into one of the high IVT synoptic types,

398   orographic storms in the central Wasatch often occur in synoptic environments not associated

399   with high IVT. NW Postfrontal LPE storms are substantially colder than the high IVT
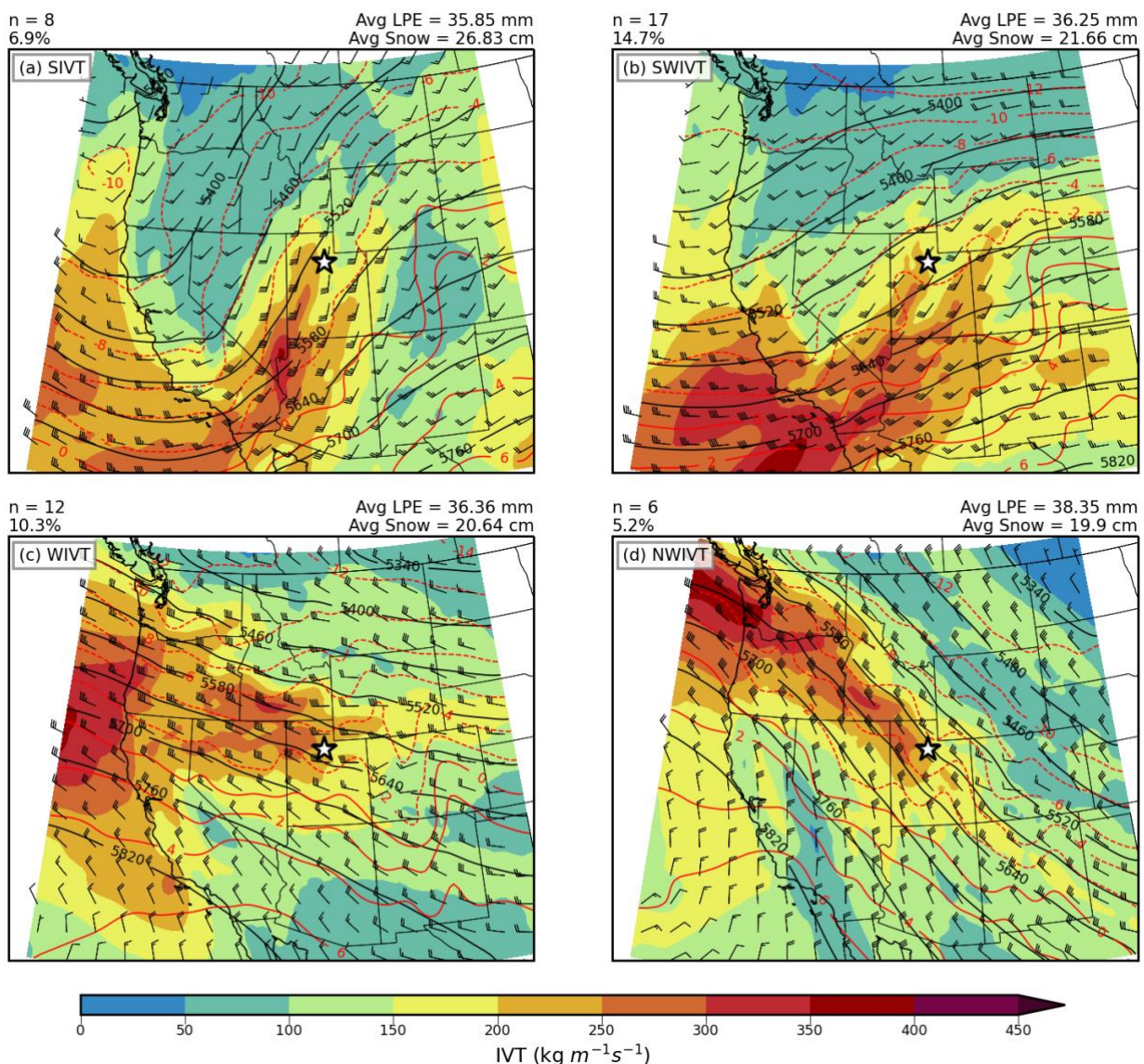

Figure 12. Composites of IVT (kg m^{-1} s^{-1}; color-fill scale at bottom), 500-hPa geopotential height (m; black contours), 700-hPa temperature (°C; red contours), and 700-hPa wind (barbs; full barb = 5 m s^{-1}) for (a) SIVT, (b) SWIVT, (c) WIVT, and (d) NWIVT LPE extremes. Number of events and percentage of all LPE extremes annotated at upper left. Average LPE and Snow annotated at upper right. Star indicates location of the study domain.

20

File generated with AMS Word template 2.0

400   synoptic types, with composite 700-hPa temperatures near -9 °C (Fig. 13a); additionally, IVT

401   values are much lower, with composite values from 50-100 kg m^{-1} s^{-1} over the central

402   Wasatch (Fig. 13a). This synoptic classification also has weaker winds that are closer to the

403   climatological wind speed frequency maximum for west-northwest and northwest flow (see

404   Fig. 7a). As evidenced by the tight packing of 700-hPa temperature contours in Arizona and

405   New Mexico (downstream of Utah), the environment is clearly post frontal (Fig. 13a). Given

406   the cold nature of NW Postfrontal storms (Figs. 9, 13a), the mean SLR for these events is
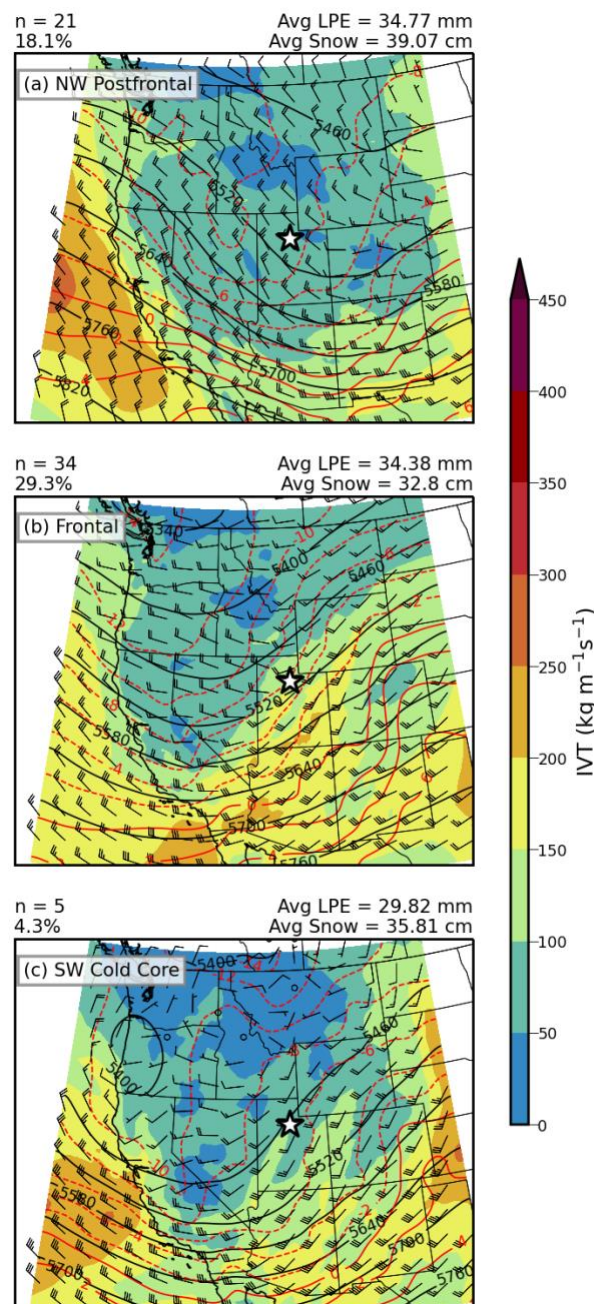

Figure 13. As in Fig. 12, but (a) NW Postfrontal, (b) Frontal, and (C) SW Cold Core LPE extremes.

407   11.5, higher than the SLR values for the high IVT synoptic types and close to median (see

408   also Fig. 8a). For snow extremes in the NW Postfrontal classification (composite not shown),

409   the mean SLR is 17.4, well above median. During Frontal events, a distinct 700-mb wind

410   shift from southwesterly to northwesterly coincident with a baroclinic zone over northern

411   Utah is indicative of a frontal trough moving through the region (Fig. 13b). These events can

412   be associated with mobile cold-frontal or quasi-stationary frontal bands. Lastly, SW Cold

413   Core events had a deep upper-level trough over the southwest and IVT < 100 kg m^{-1} s^{-1} in the

414   cold core south-southwesterly flow with 700-hPa temperatures ~ -7°C in the central Wasatch

415   (Fig. 13c). The cold nature of these events yielded a mean SLR of 11.9, higher than the mean

416   SLR for high-IVT events with southerly or southwesterly flow.

417   *d. Vapor transport diagnostics and Local Precipitation Efficiency*

418   Extreme orographic precipitation in some mountainous regions is closely related to high

419   IVT directed toward the orography (e.g., Ralph et al. 2006; Neiman et al. 2011; Rutz et al.

420   2014; Froidevaux and Martius 2016; Lorente-Plazas et al. 2018; Ralph et al. 2019). Here, we

421   present the relationships between time-integrated IVT (TIVT) and snow and LPE extremes in

422   the central Wasatch, calculating TIVT as:

$$\text{TIVT} = \int_{t_i}^{t_f} \text{IVT} \, dt, \tag{2}$$

423   where t_i and t_f are the initial and final times in a 12-h observation period, respectively. For

424   comparison purposes, a constant IVT of 250 kg m^{-1} s^{-1} over 12 h yields a TIVT of 10.8 ×10^7

425   kg m^{-1}. Snow extremes have relatively low TIVT compared to LPE extremes, with values ≤

426   0.6 × 10^7 kg m^{-1} for all but 5 events (cf. Figs. 14a,b). Snow events are most frequently NW

427   Postfrontal, which feature relatively low TIVT, as evidenced by the tight clustering of orange

428   points with northwesterly crest-level flow in Fig. 14a. The five rare high TIVT snow events

429   occurred in southerly to westerly flow (Fig. 14a).

430   LPE extremes in the central Wasatch skew towards higher TIVT compared to extreme

431   snow events, with about half featuring TIVT ≥ 0.6 × 10^7 kg m^{-1} and many falling in one of

432   the four high IVT synoptic classifications (Fig. 14b). Despite low TIVT, the NW Postfrontal

433   synoptic classification produced several LPE extremes, illustrating the relatively efficient

434   conversion of water vapor to precipitation by post-frontal orographic convection or the

435   influence of the GSL effect. One NW Postfrontal event, for instance, was one of the ten

436   largest LPE events and had TIVT ~0.2×10^7 kg m^{-1} (Fig. 14b). Similar to the low TIVT

22

437   environments associated with post-cold-frontal northwesterly flow, SW Cold Core events

438   have low TIVT, but feature southerly to southwesterly flow (Fig. 14b). The efficient

439   conversion of water vapor to precipitation in these events occurs within the unstable cold core

440   of the upper level low where orographic convection is common. Part of the reason why only

441   52 of the snow and LPE extremes are the same event is that the two types of extremes are so

442   distinct. While snow events tend to feature low TIVT and high snow-to-liquid ratios under

443   west-northwesterly to northwesterly flow, LPE extremes are often associated with high TIVT

444   and low snow-to-liquid ratios.

445   To further examine the efficiency of water vapor conversion to precipitation, we define

446   the Local Precipitation Efficiency as the ratio of LPE to TIVT:

447

448    $$\text{Local Precipitation Efficiency} = \frac{\text{LPE}}{\text{TIVT}}. \qquad (3)$$

449   This ratio is equivalent to the drying ratio that has been used to quantify airmass

450   transformation over mountain barriers (e.g., Smith et al. 2003, Kirshbaum and Smith 2008,

451   and Eidhammer et al. 2018) except that the control volume encloses a unit surface area (i.e., 1

452   m^2) rather than an entire mountain barrier. Due to this difference in volume, Local

453   Precipitation Efficiency magnitudes are several orders of magnitude smaller than mountain-

454   barrier drying ratios. We use the phrase Local Precipitation Efficiency because our focus here

455   is on the local conversion of water vapor flux to precipitation rather than the airmass
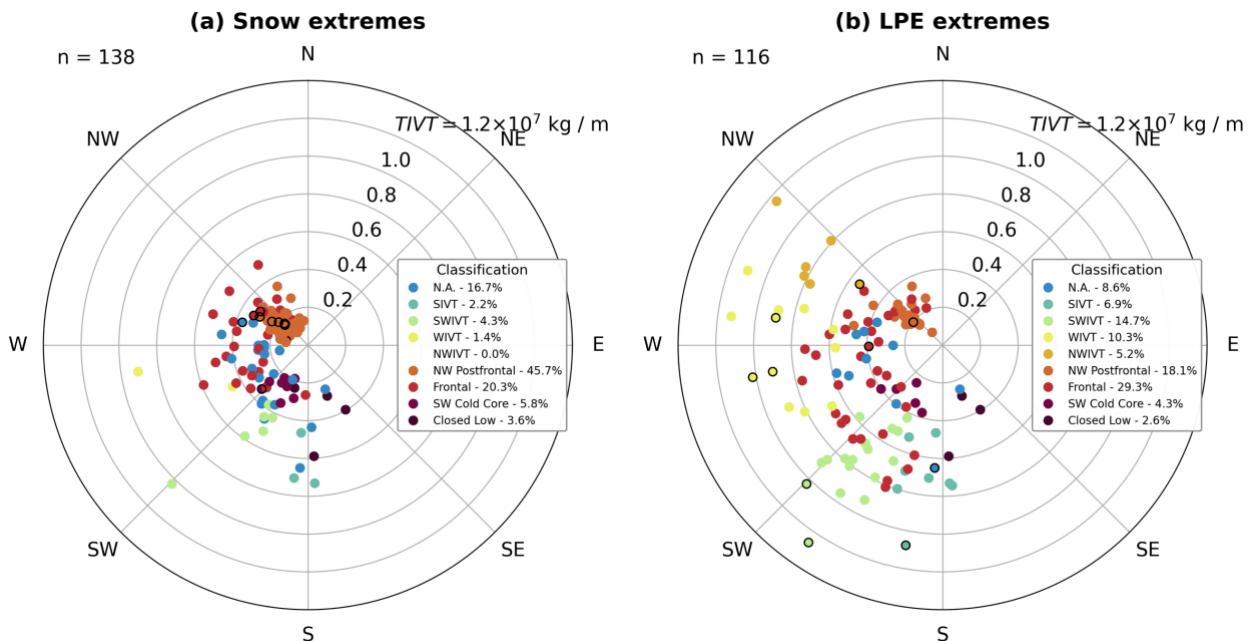

Figure 14. Polar plots of TIVT and 700-hPa wind direction for all (a) snow extremes and (b) LPE extremes colored by synoptic classification. The ten largest events are outlined in black.

456 transformation across a mountain barrier. Similarly, Eidhammer et al. (2018) used

457 precipitation efficiency synonymously with the drying ratio for mountain ranges in Colorado.

458 We note, however, that this precipitation efficiency definition is not equivalent to other

459 precipitation efficiency definitions such as the ratio of precipitation to condensate [i.e., the

460 fraction of condensate that reaches the ground as precipitation (e.g., Kirshbaum and Smith

461 2008; Narsey et al. 2019)], the ratio of precipitation to the sum of vapor convergence and

462 surface evaporation (e.g., Sui et al. 2007), or the ratio of precipitation to integrated water

463 vapor (Bordi et al. 2015).

464   For snow and LPE extremes, the median Local Precipitation Efficiency is highest when

465 the 700-hPa flow direction is west-northwesterly or northwesterly (Figs. 15a,b). Many of

466 these periods feature post-frontal orographic or GSL-effect convection that efficiently

467 generates snowfall despite low TIVT (Figs. 15a,b). The difference in median Local

468 Precipitation Efficiency between west-northwesterly or northwesterly flow and all other

469 directions except westerly is statistically significant for both snow and LPE extremes. For

470 LPE extremes the difference is also significant for westerly flow. The two outlier events in

471 west-northwesterly and northwesterly flow with Local Precipitation Efficiency $> 3.5 \times 10^{-5}$

472 occurred during a lake-effect storm in October 2010. Such lake influences are not resolved by

473 the ERA5 and serve as a non-orographic precipitation forcing mechanism that is not

474 adequately accounted for by TIVT, which is more applicable to orographic precipitation.
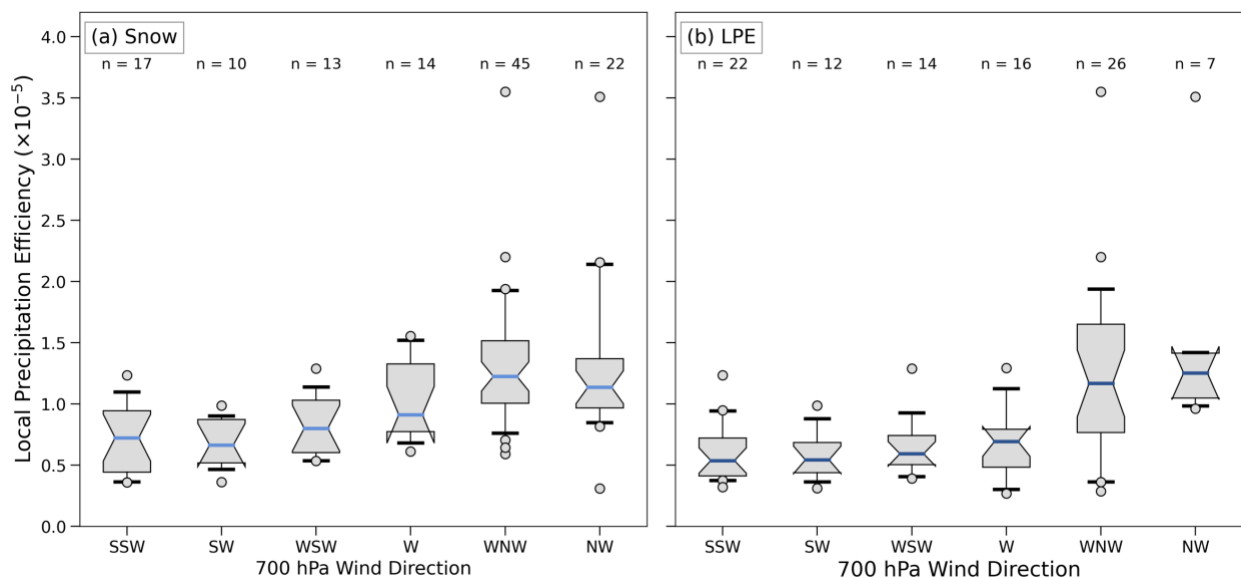

Figure 15. As in Fig. 8, but for Local Precipitation Efficiency.

475   *e. Relationship between high IVT and LPE*

476   The above results and prior research (e.g. Rutz et al. 2014; their Fig. 2a) indicate limited

477   linkages and relatively low correlations between IVT and LPE or snow in the central

478   Wasatch. Extreme LPE can be produced during periods with high *or* low IVT or TIVT (Fig.

479   14b). In this section, we examine if climatologically high IVT is a good indicator of an LPE

480   extreme, focusing on periods when IVT ≥ 200 kg m^{-1} s^{-1} in the central Wasatch (roughly the

481   99th percentile of IVT for that location) at the mid-point of a 12-h observing period. There

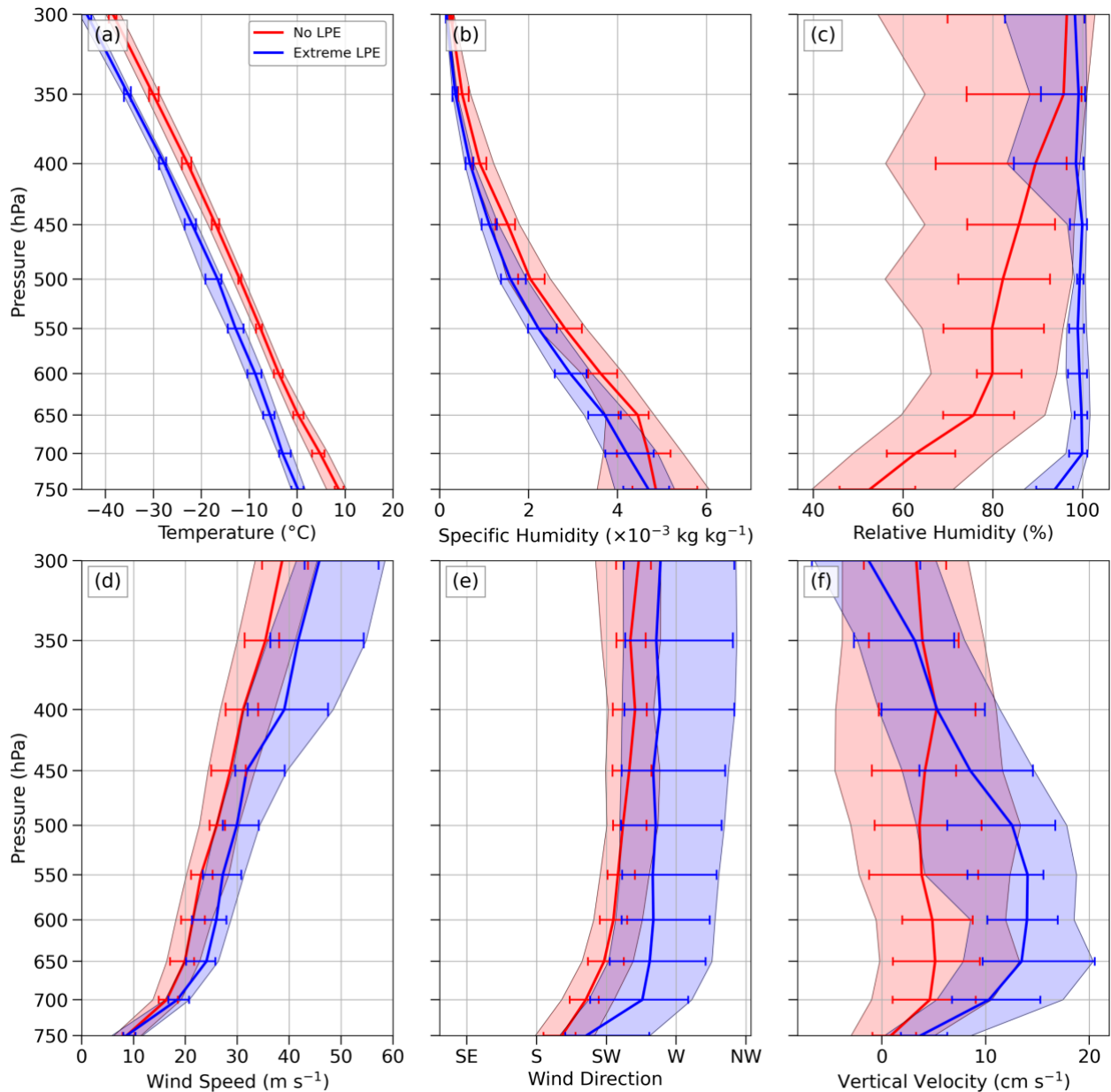482   were 112 of such periods and 37 produced *no* LPE at CLN, while only 19 resulted in an LPE

Figure 16. Atmospheric profiles for periods with IVT ≥ 200 kg m^{-1} s^{-1} and no LPE (red; n = 37) and extreme LPE (blue; n = 19) at CLN. Solid colored lines indicate median values and shading indicates interquartile range. The whiskers show the 95 percent confidence interval of the median, based on bootstrap resampling with 5000 samples. (a) Temperature. (b) Wind speed. (c) Wind direction. (d) Relative humidity. (e) Specific humidity. (f) Vertical velocity.

File generated with AMS Word template 2.0

483   extreme. Thus, climatologically high IVT alone is not sufficient to anticipate an LPE extreme

484   at CLN.

485   To understand what distinguishes high-IVT LPE extremes from those with no

486   precipitation, we compared atmospheric profiles from the two event types. High IVT periods

487   that produced extreme LPE were colder than those that did not produce LPE, with median

488   temperatures ~10°C lower throughout the atmosphere for the former, a difference that was

489   statistically significant throughout the entire atmospheric column (Fig. 16a). Consistent with

490   these lower temperatures, the high IVT periods that produced extreme LPE featured lower

491   specific humidity but higher relative humidity, the difference in the latter being statistically

492   significant up to 425 hPa (Fig. 16b,c). The larger subsaturations in high IVT periods which

493   produced no LPE are simply less favorable for precipitation development, despite the high

494   IVT. The high IVT extreme LPE events also had higher wind speeds, although the difference

495   was not statistically significant (Fig. 16d). In both cases, low level winds (i.e., below ~650

496   hPa) veer with height, consistent with warm-air advection if the flow is near geostrophic, but

497   events with precipitation have a stronger meridional component and thus may be less

498   influenced by the Oquirrh Range to the west, though that difference is not statistically

499   significant (Fig. 16e). Lastly, vertical velocities are shifted toward higher upward values

500   during high IVT periods that produce extreme LPE, especially near and above crest level

501   (~650-600 hPa), where the differences are statistically significant (Fig. 16f). The ~31 km grid

502   spacing of the ERA5 does not resolve the narrow Wasatch Range. Instead, a gradual slope

503   extends across much of northern Utah. Therefore, we suggest that this enhanced upward

504   motion reflects Rossby wave and frontogenetical forcing during extreme LPE periods (Fig.

505   16f). In summary, climatologically high IVT in the central Wasatch can be associated with

506   extreme precipitation, but it is not a sufficient condition and can be associated with a wide

507   range of possible outcomes. Additional environmental factors are needed to produce extreme

508   LPE, including a near-saturated environment and large-scale ascent.

509   *f. Radar characteristics*

510   We conclude our analysis by presenting statistics from the KMTX radar. We produced

511   plots of the frequency of 0.5° radar echoes ≥ 10 dBZ for both snow and LPE extremes,

512   binned by either 700-hPa flow direction or synoptic classification. The structure of these plots

513   was similar for both snow and LPE extremes, so for brevity, we present LPE extremes.

514   During periods with south-southwesterly and southwesterly flow, echo frequencies are

26

515 highest over the Wasatch Range and down-radial areas not affected by beam blockage to the

516 east. Relatively high echo frequencies are also present over the Stansbury and Oquirrh

517 Ranges and in some surrounding lowland areas (Fig. 17a,b). The lowlands immediately west

518 of the Wasatch Range also exhibit higher frequencies, although the Stansbury and Oquirrh

519 Ranges and/or the Traverse Ranges between the Stansbury and Oquirrh Ranges or Oquirrh

520 and Wasatch Ranges appear to produce some precipitation shadowing, in the form of reduced

521 echo frequencies, over portions of the Tooele and Salt Lake Valleys (see Fig. 1b for

522 geographic features). This suggests that these events frequently occur in the presence of a

523 broader-scale precipitation system with embedded orographic precipitation enhancement over

524 the Wasatch and other mountain ranges and lowland precipitation rates modulated by local

525 terrain features. In west-southwesterly flow, high echo frequencies cover a broad region, with

526 less modulation between the mountains and the lowlands, consistent with the presence of a

527 front or large-scale forcing (Fig. 17c). In westerly flow, echo frequencies are greatest over the

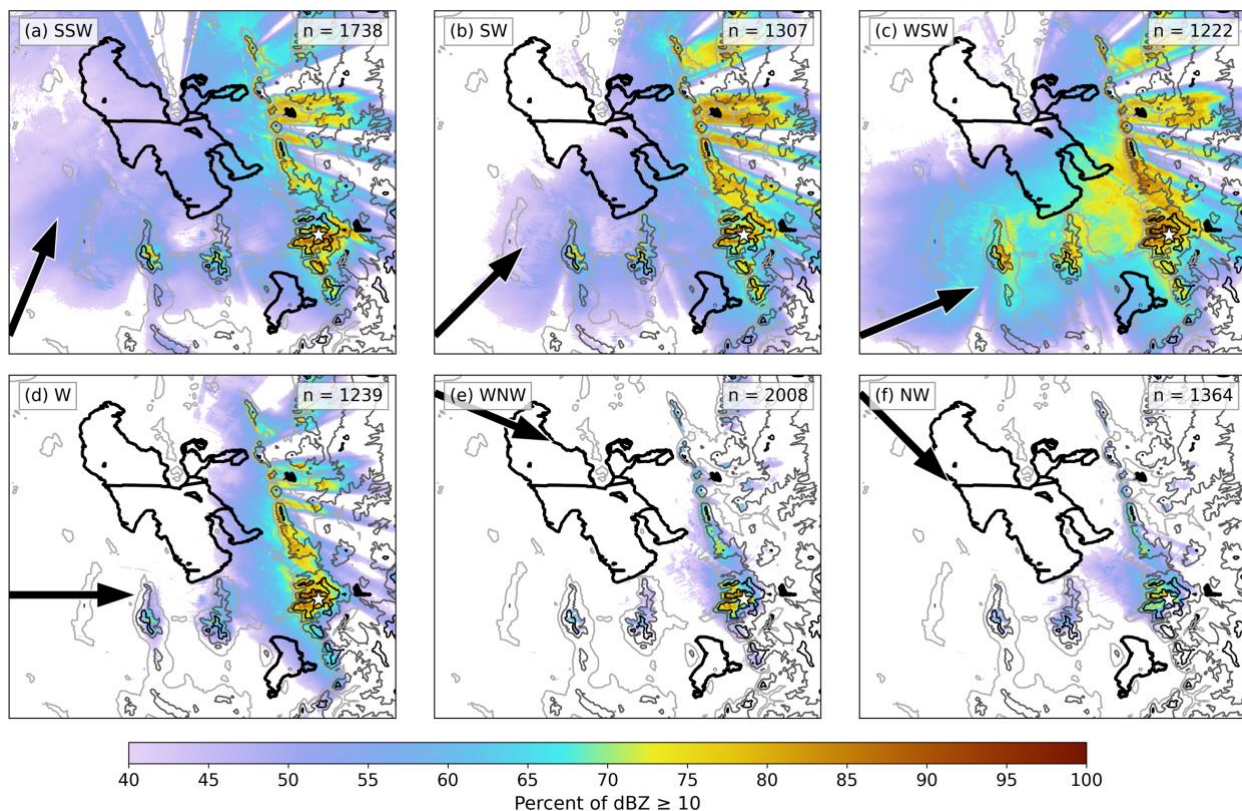528 Stansbury, Oquirrh, and Wasatch Ranges; lowlands to the immediate west (i.e., upstream) of

Figure 17. Frequency of 0.5° radar echoes ≥ 10 dBZ (%; scale at bottom) for radar scans occurring during LPE extremes with (a) south-southwesterly, (b) southwesterly, (c) west-southwesterly, (d) westerly, (e) west-northwesterly, and (f) northwesterly 700-hPa winds. Thick black lines outline lakes. Thin contours display terrain height every 500 m from 1200–2700 m MSL. Black arrow displays the prevailing 700-hPa flow direction and the white star denotes CLN. The number of radar scans used to produce the plot is in the upper right corner.

File generated with AMS Word template 2.0

529   the Wasatch Range; and down-radial areas to the east of the Wasatch Range not affected by

530   beam blockage (Fig 17d). Enhanced echo frequencies in the lowlands upstream of the

531   Wasatch may reflect the influence of terrain-trapped airflows related to blocking and other

532   orographic processes or upstream tilting mountain waves (e.g., Neiman et al. 2002; Cox et al.

533   2005; Colle et al. 2005; Valenzuela and Kingsmill 2015, 2017; Ryoo et al. 2020), with some

534   modulation by the upstream Stansbury and Oquirrh Ranges (e.g., see the lower echo

535   frequency immediately east and downstream of the Stansbury and Oquirrh Ranges). Finally,

536   for west-northwesterly and northwesterly flow, echoes are more confined to over the central

537   Wasatch and the lowland region *immediately upstream* (Fig. 17d,e), indicating highly

538   localized enhancement of post-frontal orographic or lake-effect convection.

539   The frequency of 0.5° radar echoes $\geq$ 10 dBZ for each synoptic classification provides

540   another perspective. During the SIVT and NWIVT events the greatest frequency of radar

541   echoes $\geq$ 10 dBZ is in the Wasatch Range (Figs. 18a,d). In the case of SIVT, echo

542   frequencies are much higher in the central Wasatch than in the northern or southern Wasatch
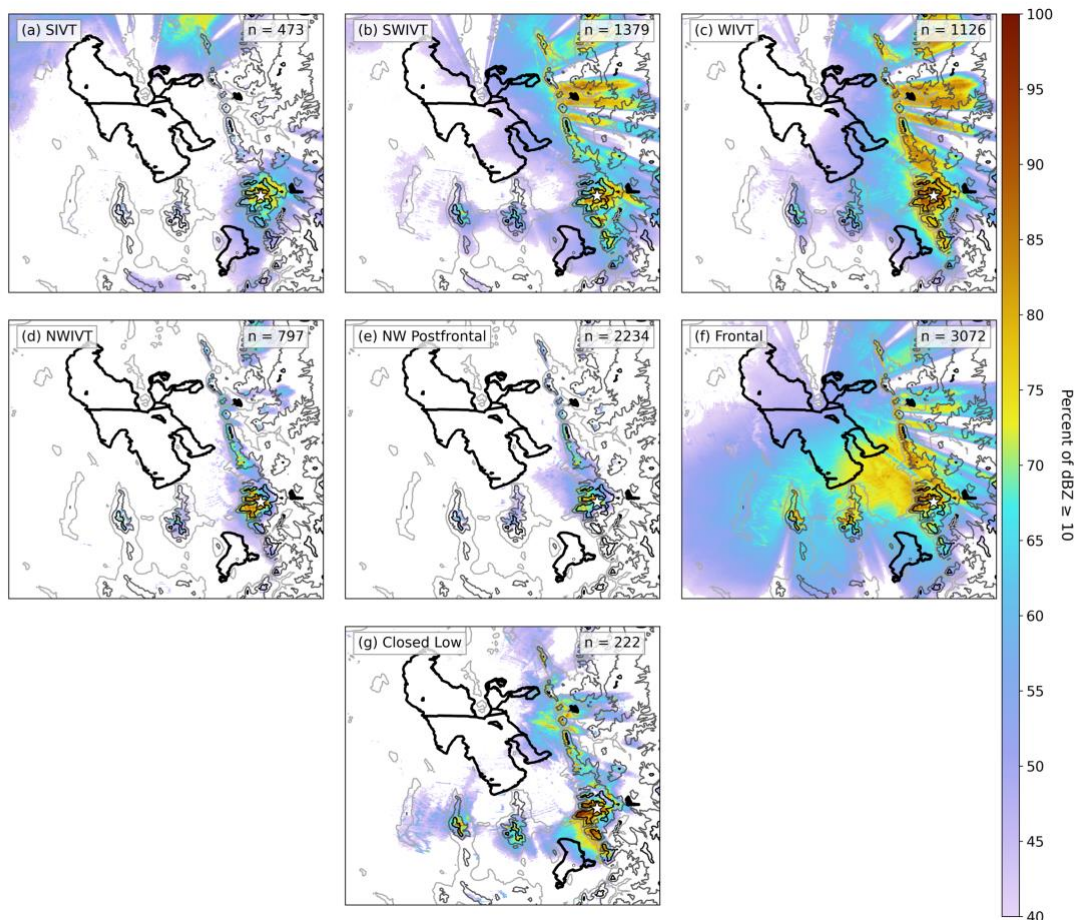

Figure 18. As in Fig. 17 but for the (a) SIVT, (b) SWIVT, (c) WIVT, (d) NWIVT, (e) NW Postfrontal, (f) Frontal, and (g) SW Cold Core synoptic classifications.

543   Range. During the SWIVT and WIVT periods, the Wasatch Range still features the highest

544   echo frequencies, but the echo frequencies are also locally high over portions of the

545   Stansbury and Oquirrh ranges and during WIVT there is significant coverage in the lowlands

546   well upstream of the Wasatch Range (cf. Figs. 18b,c and 18a,d). NW Postfrontal storms have

547   radar echoes confined to over and immediately upstream of the central Wasatch, (Fig. 18e);

548   the radar structure for these storms is similar to the plots for west-northwesterly and

549   northwesterly flow (Figs. 17e,f) indicating the predominance of orographic and lake-effect

550   convection during these periods and relatively infrequent concurrent occurrence of synoptic

551   precipitation features. This is broadly consistent with Alcott et al. (2012) who found that

552   GSL-effect precipitation occurred concurrently with synoptic stratiform precipitation only

553   10% of the time. Frontal events have the greatest coverage of $\geq$ 10 dBZ echoes with small

554   variations between mountains and lowland areas (Fig. 18f). Thus, many of the Frontal events

555   likely feature high LPE rates in the valleys as well as the mountains, consistent with

556   Steenburgh (2003). The SW Cold Core statistics show enhancement over the Oquirrh,

557   Stansbury and Wasatch Ranges, as well as over the lowlands upstream of the central Wasatch

558   (over Utah Valley) and the northern Wasatch (Fig 18g).

559   The radar statistics described above indicate varied orographic and large-scale

560   contributions to LPE extremes at CLN. Echo frequencies suggest many SIVT, SWIVT,

561   NWIVT, and NW Postfrontal events feature relatively strong and, for some flow directions,

562   localized enhancement of precipitation over and just upstream of the central Wasatch. In

563   contrast, during WIVT and especially Frontal events, valley and lowland echo frequencies are

564   higher, suggesting an important contribution from large-scale forcing. Although not a focus

565   of this research, the above analyses also provide insights into the modulation of lowland

566   precipitation, which can be confined to near the central Wasatch during the SIVT, SWIVT,

567   NWIVT, and NW Postfrontal periods, but exhibit wide coverage during periods with stronger

568   large-scale forcing.

4. Conclusions

570   Using snow and LPE observations from the Alta-Collins snow study plot (CLN) at Alta

571   Ski Area, this research examined the characteristics of extreme snowfall events in northern

572   Utah's upper Little Cottonwood Canyon (LCC), which can contribute to dangerous avalanche

573   conditions that force the closure of State Route 210 (SR-210) and threaten lives and property

574   in the Town of Alta and Village of Snowbird. During the 2000–2022 cool-season (October–

575   April) study period, there was an average of 117.7 12-h periods with ≥ 2.54 cm of new snow

576   at CLN, the largest of which produced nearly 65 cm of snow. Almost all precipitation at CLN

577   falls as snow during the cool season, with median snow-to-liquid ratios (SLR) of 12.8,

578   characteristic of an intermountain snow climate. Extreme events, defined as the 95th

579   percentile of 12-h new snow or liquid precipitation equivalent (LPE), exceeded 30.5 cm and

580   27.9 mm, respectively.

581   A wide range of flow directions are associated with extreme snowfall events in upper

582   LCC. Snow extremes occur most frequently in west-northwesterly and northwesterly flow,

583   while LPE extremes exhibit a bimodality in the flow direction frequency, with maxima for

584   west-northwesterly and south-southwesterly flow. The LPE extreme bimodality contrasts

585   with the modal distribution found over some broad, quasi-linear mountain barriers like the

586   Cascade Range or Sierra Nevada (e.g., Pandey et al. 1999, see their Fig. 5; Yuter et al. 2011,

587   see their Fig. 2) and appears to reflect shadowing by the Stansbury and Oquirrh ranges to the

588   west, the influence of the Great Salt Lake and terrain-forced convergence due to the presence

589   of the Oquirrh Range during northwesterly flow (Alcott and Steenburgh 2013), and the three-

590   dimensional topography of the central Wasatch, which includes zonally oriented sub-barrier

591   ridges that yield upslope flow from a wide range of flow directions. The primacy of the west-

592   northwesterly to northwesterly flow maximum for snow extremes reflects SLR, which is

593   higher in west-northwesterly to northwesterly storms due to the lower temperatures

594   associated with those flow directions.

595   Heavy snowfall in LCC is produced by diverse synoptic patterns. We identified eight

596   synoptic classifications that generate snowfall extremes including four associated with high

597   IVT from the south, southwest, west, and northwest (SIVT, SWIVT, WIVT, and NWIVT,

598   respectively), post-cold-frontal northwesterly flow (NW Postfrontal), cold fronts or baroclinic

599   troughs (Frontal), south-southwesterly cold core flow (SW Cold Core) and closed low

600   pressure systems (Closed Low). IVT penetration for the high IVT patterns occurs to the north

601   or south of the southern high Sierra and features relatively high 700-hPa (crest-level) winds

602   and temperatures, which, despite producing high LPE, frequently leads to modest snowfall

603   totals due to low SLRs. Snow extremes occur most frequently during NW Postfrontal periods

604   that are colder and often feature high SLRs.

605   Although some other mountainous regions such as California have a relatively high

606   correlation between integrated water vapor transport (IVT) and LPE (e.g. Dettinger et al.

607   2011; Ricciotti and Cordeira 2022), the correlation over the western interior of the contiguous

608   western U.S. is relatively low (see Rutz et al. 2014, their Fig. 2a). This more limited

609   relationship between IVT and LPE is reflected in our analysis. Of the 112 periods with IVT ≥

610   200 kg m^{-1} s^{-1} (roughly the 99th percentile) at the mid-point of a 12-h observing period, only

611   19 produced an LPE extreme and 37 produced *no* LPE at CLN. Comparison of events with

612   these two outcomes indicates additional environmental factors are needed to produce extreme

613   LPE, including a near-saturated environment (often with lower temperatures) and large-scale

614   ascent. Additionally, in upper LCC storms with low IVT can produce snow and LPE

615   extremes, especially during NW Postfrontal events. The Local Precipitation Efficiency,

616   defined as the ratio of precipitation to time-integrated IVT expressed as a water depth, is

617   especially high during these periods, consistent with the efficient conversion of water vapor

618   to precipitation in orographic convection or lake-effect storms.

619   Conditional radar statistics based on flow direction or synoptic classification indicate

620   varied orographic and large-scale contributions to LPE extremes at CLN. Radar echo

621   frequencies indicate localized enhancement of precipitation over and just upstream of the

622   central Wasatch during SIVT, SWIVT, NWIVT, and NW Postfrontal events, whereas

623   broader coverage occurs during WIVT and especially Frontal periods. In the case of the

624   latter, the contrast in echo frequency from lowland to upland areas is relatively small,

625   indicating that frontal periods exhibit weaker contrasts between lowland and mountain

626   precipitation.

627   Although this research focused on the central Wasatch, it has broader implications for

628   understanding orographic precipitation in other mountainous regions. Much of the prior work

629   on orographic precipitation has focused on broad, quasilinear mountain ranges and

630   orographic precipitation processes are often conceptualized using a single-ridge framework.

631   The climatology for upper Little Cottonwood Canyon, however, illustrates how upstream

632   topography and three-dimensional terrain geometries can complicate storm characteristics,

633   orographic flow response, and precipitation processes. Although the Wasatch Range is

634   generally long and narrow, the terrain of the *central Wasatch* broadens and has a nearly 1:1

635   horizontal aspect ratio (see Fig. 1c). We hypothesize that this terrain geometry exposes the

636   central Wasatch to flow from multiple flow directions, with the high terrain of the northern

637   and southern Wasatch Range limiting flow splitting. As a result, local orographic

638   precipitation enhancement and extremes occur across a wide range of flow directions.

639   Upstream ranges (i.e., the Oquirrh and Stansbury Ranges), however, may limit the frequency

640   of snowfall extremes during flow traversing those barriers. Finally, we illustrate that over

641   interior mountainous regions, the relationship between IVT and precipitation may not be

31

642 straightforward and show that during unstable post-frontal periods, the efficient conversion of

643 water vapor to snow can lead to high snowfall rates despite relatively low IVT.

644   Overall, these results extend prior research by comprehensively describing the

645 characteristics of extreme snowfall events in upper LCC, illustrating the meteorology

646 associated with these events from an LPE *and* snow perspective, and describing the complex

647 linkages between IVT and LPE extremes at this *interior* mountain location. These results

648 have implications for weather forecasting, avalanche hazard assessment, and road-weather

649 maintenance in LCC. While this research elucidated the climatological characteristics of

650 extreme snowfall in upper LCC, it does not provide insight into the *physical mechanisms*

651 responsible for the heavy snowfall. Future work is needed to better understand these

652 precipitation processes, including multi-ridge effects associated with broadly separated,

653 serially arranged mountain ridges commonly found in the Great Basin (e.g., the Stansbury,

654 Oquirrh, and Wasatch Ranges) and finer-scale ridge-canyon corrugations within individual

655 ranges (e.g., the Alpine, Cottonwood, and Wildcat Ridges in the Central Wasatch). This

656 could involve the use of high-resolution numerical simulations and collection of airborne

657 cloud-radar observations to gaiFign an understanding of the hydrometeor growth, transport,

658 and fallout processes that make upper LCC one of the snowiest places in the interior western

659 United States.

669 *Data Availability Statement.*

670   The CLN snow observations used in this research are openly available from the

671 University of Utah Research Data Repository (Wasserstein and Steenburgh 2023). The ERA5

672 reanalysis is available from the Copernicus Climate Change Service (Hersbach et al.

File generated with AMS Word template 2.0

673   2018a,b). The NEXRAD radar data are available from Amazon Web Services (NOAA 1991;

674   https://registry.opendata.aws/noaa-nexrad/).

REFERENCES

676   Alcott, T. I., and W. J. Steenburgh, 2013: Orographic Influences on a Great Salt Lake–Effect
677   Snowstorm. *Mon. Wea. Rev.*, **141**, 2432–2450, https://doi.org/10.1175/MWR-D-12-
678   00328.1.

679   ——, ——, and N. F. Laird, 2012: Great Salt Lake–Effect Precipitation: Observed
680   Frequency, Characteristics, and Associated Environmental Factors. *Wea. Forecasting*,
681   **27**, 954–971, https://doi.org/10.1175/WAF-D-12-00016.1.

682   Blattenberger, G., and R. Fowles, 1995: Road closure to mitigate avalanche danger: a case
683   study for Little Cottonwood Canyon. *Int. J. Forecast.*, **11**, 159–174,
684   https://doi.org/10.1016/0169-2070(94)02008-D.

685   Bjerknes, J., 1966: A possible response of the atmospheric Hadley circulation to equatorial
686   anomalies of ocean temperature. *Tellus*, **18**, 820–829, https://doi.org/10.1111/j.2153-
687   3490.1966.tb00303.x.

688   ——, 1969: ATMOSPHERIC TELECONNECTIONS FROM THE EQUATORIAL
689   PACIFIC. *Monthly Weather Review*, **97**, 163–172, https://doi.org/10.1175/1520-
690   0493(1969)097<0163:ATFTEP>2.3.CO;2.

691   Bordi, I., X. Zhu, and K. Fraedrich, 2016: Precipitable water vapor and its relationship with
692   the Standardized Precipitation Index: ground-based GPS measurements and reanalysis
693   data. *Theor Appl Climatol*, **123**, 263–275, https://doi.org/10.1007/s00704-014-1355-0.

694   Campbell, L. S., W. J. Steenburgh, Y. Yamada, M. Kawashima, and Y. Fujiyoshi, 2018:
695   Influences of Orography and Coastal Geometry on a Transverse-Mode Sea-Effect
696   Snowstorm over Hokkaido Island, Japan. *Mon. Wea. Rev.*, **146**, 2201–2220,
697   https://doi.org/10.1175/MWR-D-17-0286.1.

698   Capozzi, V., C. De Vivo, and G. Budillon, 2022: Synoptic control over winter snowfall
699   variability observed in a remote site of Apennine Mountains (Italy), 1884–2015. *The
700   Cryosphere*, **16**, 1741–1763, https://doi.org/10.5194/tc-16-1741-2022.

701   Caracena, F., R. A. Maddox, L. R. Hoxit, and C. F. Chappell, 1979: Mesoanalysis of the Big
702   Thompson Storm. *Mon. Wea. Rev.*, **107**, 1–17, https://doi.org/10.1175/1520-
703   0493(1979)107<0001:MOTBTS>2.0.CO;2.

704   Carpenter, D. M., 1993: The Lake Effect of the Great Salt Lake: Overview and Forecast
705   Problems. *Wea. Forecasting*, **8**, 181–193, https://doi.org/10.1175/1520-
706   0434(1993)008<0181:TLEOTG>2.0.CO;2.

707   Casaretto, G., M. E. Dillon, P. Salio, Y. G. Skabar, S. W. Nesbitt, R. S. Schumacher, C. M.
708   García, and C. Catalini, 2022: High-Resolution NWP Forecast Precipitation
709   Comparison over Complex Terrain of the Sierras de Córdoba during RELAMPAGO-
710   CACTI. *Wea. Forecasting*, **37**, 241–266, https://doi.org/10.1175/WAF-D-21-0006.1.

711   Colle, B. A., R. B. Smith, and D. A. Wesley, 2013: Theory, Observations, and Predictions of
712   Orographic Precipitation. *Mountain Weather Research and Forecasting: Recent*
713   *Progress and Current Challenges*, F.K. Chow, S.F.J. De Wekker, and B.J. Snyder,
714   Eds., *Springer Atmospheric Sciences*, Springer Netherlands, 291–344.

715   Conlan, M., and B. Jamieson, 2016a: Naturally triggered persistent deep slab avalanches in
716   western Canada Part I: avalanche characteristics and weather trends from weather
717   stations. *J. Glaciol.*, **62**, 243–255, https://doi.org/10.1017/jog.2016.1.

718   ——, and ——, 2016b: Naturally triggered persistent deep slab avalanches in western
719   Canada Part II: weather trends from model forecasts. *J. Glaciol.*, **62**, 256–269,
720   https://doi.org/10.1017/jog.2016.2.

721   DeHart, J. C., and R. A. Houze, 2017: Orographic Modification of Precipitation Processes in
722   Hurricane Karl (2010). *Mon. Wea. Rev.*, **145**, 4171–4186,
723   https://doi.org/10.1175/MWR-D-17-0014.1.

724   Dettinger, M. D., F. M. Ralph, T. Das, P. J. Neiman, and D. R. Cayan, 2011: Atmospheric
725   Rivers, Floods and the Water Resources of California. *Water*, **3**, 445–478,
726   https://doi.org/10.3390/w3020445.

727   Dunn, L. B., 1983: Quantitative and Spacial Distribution of Winter Precipitation Along
728   Utah's Wasatch Front. *NOAA Technical Memorandum*,.

729   Eidhammer, T., V. Grubišić, R. Rasmussen, and K. Ikdea, 2018: Winter Precipitation
730   Efficiency of Mountain Ranges in the Colorado Rockies Under Climate Change. *J.*
731   *Geophys. Res.: Atmospheres*, **123**, 2573–2590,
732   https://doi.org/10.1002/2017JD027995.

733   Farestveit, N., and S. Skutlaberg, 2009: Experiences on a Storm Causing Avalanche Cycles in
734   South-West Norway. *International Snow Science Workshop, Davos 2009,*
735   *Proceedings*, 567–571.

736   Foehn, P., M. Stoffel, and P. Bartelt, 2002: Formation and forecasting of large (catastrophic)
737   new snow avalanches. *International snow science workshop proceedings 2002*, 141–
738   148.

739   Foresti, L., I. V. Sideris, L. Panziera, D. Nerini, and U. Germann, 2018: A 10-year radar-
740   based analysis of orographic precipitation growth and decay patterns over the Swiss
741   Alpine region. *Quart. J. Roy. Meteor. Soc.*, **144**, 2277–2301,
742   https://doi.org/10.1002/qj.3364.

743   Froidevaux, P., and O. Martius, 2016: Exceptional integrated vapour transport toward
744   orography: an important precursor to severe floods in Switzerland. *Quart. J. Roy.*
745   *Meteor. Soc.*, **142**, 1997–2012, https://doi.org/10.1002/qj.2793.

746   Hersbach, H., and Coauthors, 2018a: ERA5 hourly data on pressure levels from 1959 to
747   present. Copernicus Climate Change Service (C3S) Climate Data Store (CDS),
748   accessed 3 February 2023, https://doi.org/10.24381/cds.bd0915c6.
749

File generated with AMS Word template 2.0

Hersbach, H., and Coauthors, 2018b: ERA5 hourly data on single levels from 1959 to present. Copernicus Climate Change Service (C3S) Climate Data Store (CDS), accessed 3 February 2023, https://doi.org/10.24381/cds.adbb2d47.

Hersbach, H., and Coauthors, 2020: The ERA5 global reanalysis. *Quart. J. Roy. Meteor. Soc.*, **146**, 1999–2049, https://doi.org/10.1002/qj.3803.

Hilker, N., A. Badoux, and C. Hegg, 2009: The Swiss flood and landslide damage database 1972–2007. *Nat. Hazards Earth Syst. Sci.*, **9**, 913–925, https://doi.org/10.5194/nhess-9-913-2009.

Horel, J. D., and J. M. Wallace, 1981: Planetary-Scale Atmospheric Phenomena Associated with the Southern Oscillation. *Monthly Weather Review*, **109**, 813–829, https://doi.org/10.1175/1520-0493(1981)109<0813:PSAPAW>2.0.CO;2.

——, and C. V. Gibson, 1994: Analysis and Simulation of a Winter Storm over Utah. *Wea. Forecasting*, **9**, 479–494, https://doi.org/10.1175/1520-0434(1994)009<0479:AASOAW>2.0.CO;2.

Houze Jr., R. A., 2012: Orographic effects on precipitating clouds. *Rev. Geophys.*, **50**, https://doi.org/10.1029/2011RG000365.

Houze Jr, R. A., C. N. James, and S. Medina, 2001: Radar observations of precipitation and airflow on the Mediterranean side of the Alps: Autumn 1998 and 1999. *Quart. J. Roy. Meteor. Soc.*, **127**, 2537–2558, https://doi.org/10.1002/qj.49712757804.

Jag, J., 2023: Avalanche chaos causes Cottonwood Canyon closures, strands thousands. *Salt Lake Tribune*, April 5.

James, C. N., and R. A. Houze, 2005: Modification of Precipitation by Coastal Orography in Storms Crossing Northern California. *Mon. Wea. Rev.*, **133**, 3110–3131, https://doi.org/10.1175/MWR3019.1.

Johnston, E. C., F. V. Davenport, L. Wang, J. K. Caers, S. Muthukrishnan, M. Burke, and N. S. Diffenbaugh, 2021: Quantifying the Effect of Precipitation on Landslide Hazard in Urbanized and Non-Urbanized Areas. *Geophys. Res. Lett.*, **48**, e2021GL094038, https://doi.org/10.1029/2021GL094038.

Kirshbaum, D. J., and R. B. Smith, 2008: Temperature and moist-stability effects on midlatitude orographic precipitation. *Quart. J. Roy. Meteor. Soc.*, **134**, 1183–1199, https://doi.org/10.1002/qj.274.

Lackmann, G. M., and J. R. Gyakum, 1999: Heavy Cold-Season Precipitation in the Northwestern United States: Synoptic Climatology and an Analysis of the Flood of 17–18 January 1986. *Wea. Forecasting*, **14**, 687–700, https://doi.org/10.1175/1520-0434(1999)014<0687:HCSPIT>2.0.CO;2.

Lavers, D. A., and G. Villarini, 2013: The nexus between atmospheric rivers and extreme precipitation across Europe. *Geophys. Res. Lett.*, **40**, 3259–3264, https://doi.org/10.1002/grl.50636.

789 Lentink, H. S., C. M. Grams, M. Riemer, and S. C. Jones, 2018: The Effects of Orography on
790   the Extratropical Transition of Tropical Cyclones: A Case Study of Typhoon Sinlaku
791   (2008). *Mon. Wea. Rev.*, **146**, 4231–4246, https://doi.org/10.1175/MWR-D-18-
792   0150.1.

793 Liu, M., and J. A. Smith, 2016: Extreme Rainfall from Landfalling Tropical Cyclones in the
794   Eastern United States: Hurricane Irene (2011). *J. Hydrometeor.*, **17**, 2883–2904,
795   https://doi.org/10.1175/JHM-D-16-0072.1.

796 Lorente-Plazas, R., T. P. Mitchell, G. Mauger, and E. P. Salathé, 2018: Local Enhancement
797   of Extreme Precipitation during Atmospheric Rivers as Simulated in a Regional
798   Climate Model. *J. Hydrometeor.*, **19**, 1429–1446, https://doi.org/10.1175/JHM-D-17-
799   0246.1.

800 Maddox, R. A., L. R. Hoxit, C. F. Chappell, and F. Caracena, 1978: Comparison of
801   Meteorological Aspects of the Big Thompson and Rapid City Flash Floods. *Mon.*
802   *Wea. Rev.*, **106**, 375–389, https://doi.org/10.1175/1520-
803   0493(1978)106<0375:COMAOT>2.0.CO;2.

804 Manabe, S., 1957: On the Modification of Air-mass over the Japan Sea when the Outburst of
805   Cold Air Predominates. *J. Meteor. Soc. Japan. Ser. II*, **35**, 311–326,
806   https://doi.org/10.2151/jmsj1923.35.6_311.

807 Martinez-Villalobos, C., and J. D. Neelin, 2019: Why Do Precipitation Intensities Tend to
808   Follow Gamma Distributions? *J. Atmos. Sci.*, **76**, 3611–3631,
809   https://doi.org/10.1175/JAS-D-18-0343.1.

810 McMillen, J. D., and W. J. Steenburgh, 2015a: Impact of Microphysics Parameterizations on
811   Simulations of the 27 October 2010 Great Salt Lake–Effect Snowstorm. *Wea.*
812   *Forecasting*, **30**, 136–152, https://doi.org/10.1175/WAF-D-14-00060.1.

813 ——, and ——, 2015b: Capabilities and Limitations of Convection-Permitting WRF
814   Simulations of Lake-Effect Systems over the Great Salt Lake. *Wea. Forecasting*, **30**,
815   1711–1731, https://doi.org/10.1175/WAF-D-15-0017.1.

816 Minder, J. R., D. R. Durran, G. H. Roe, and A. M. Anders, 2008: The climatology of small-
817   scale orographic precipitation over the Olympic Mountains: Patterns and processes.
818   *Quart. J. Roy. Meteor. Soc.*, **134**, 817–839, https://doi.org/10.1002/qj.258.

819 Mock, C. J., and K. W. Birkeland, 2000: Snow Avalanche Climatology of the Western
820   United States Mountain Ranges. *Bulletin of the American Meteorological Society*, **81**,
821   2367–2392, https://doi.org/10.1175/1520-0477(2000)081<2367:SACOTW>2.3.CO;2.

822 Nalli, B., and M. Mckee, 2018: How Little Cottonwood Canyon got this way and what can be
823   done to fix it. *International Snow Science Workshop Proceedings 2018, Innsbruck,*
824   *Austria*, 246–250.

825 Narsey, S., C. Jakob, M. S. Singh, M. Bergemann, V. Louf, A. Protat, and C. Williams, 2019:
826   Convective Precipitation Efficiency Observed in the Tropics. *Geophys. Res. Lett.*, **46**,
827   13574–13583, https://doi.org/10.1029/2019GL085031.

828 NCEI, 2021: U.S. Climate Normals. *National Centers for Environmental Information*
829   *(NCEI),*. https://www.ncei.noaa.gov/products/land-based-station/us-climate-normals
830   (Accessed April 14, 2023).

831 Neiman, P. J., L. J. Schick, F. M. Ralph, M. Hughes, and G. A. Wick, 2011: Flooding in
832   Western Washington: The Connection to Atmospheric Rivers. *J. Hydrometeor.*, **12**,
833   1337–1358, https://doi.org/10.1175/2011JHM1358.1.

834 NOAA National Weather Service, 1991: NOAA Next Generation Radar(NEXRAD) Level II
835   Base Data. https://doi.org/10.7289/V5W9574V.
836
837 Nöthiger, C., and H. Elsasser, 2004: Natural Hazards and Tourism: New Findings on the
838   European Alps. *mred*, **24**, 24–27, https://doi.org/10.1659/0276-
839   4741(2004)024[0024:NHATNF]2.0.CO;2.

840 Pandey, G. R., D. R. Cayan, and K. P. Georgakakos, 1999: Precipitation structure in the
841   Sierra Nevada of California during winter. *J. Geophys. Res.: Atmospheres*, **104**,
842   12019–12030, https://doi.org/10.1029/1999JD900103.

843 Ralph, F. M., P. J. Neiman, G. A. Wick, S. I. Gutman, M. D. Dettinger, D. R. Cayan, and A.
844   B. White, 2006: Flooding on California's Russian River: Role of atmospheric rivers.
845   *Geophys. Res. Lett.*, **33**, https://doi.org/10.1029/2006GL026689.

846 ——, J. J. Rutz, J. M. Cordeira, M. Dettinger, M. Anderson, D. Reynolds, L. J. Schick, and
847   C. Smallcomb, 2019: A Scale to Characterize the Strength and Impacts of
848   Atmospheric Rivers. *Bull. Amer. Meteor. Soc.*, **100**, 269–289,
849   https://doi.org/10.1175/BAMS-D-18-0023.1.

850 Ricciotti, J. A., and J. M. Cordeira, 2022: Summarizing Relationships among Landfalling
851   Atmospheric Rivers, Integrated Water Vapor Transport, and California Watershed
852   Precipitation 1982–2019. *J. Hydrometeor.*, **23**, 1439–1454,
853   https://doi.org/10.1175/JHM-D-21-0119.1.

854 Roe, G. H., 2005: Orographic Precipitation. *Annu. Rev. Earth Planet. Sci.*, **33**, 645–671,
855   https://doi.org/10.1146/annurev.earth.33.092203.122541.

856 Roebber, P. J., and J. R. Gyakum, 2003: Orographic Influences on the Mesoscale Structure of
857   the 1998 Ice Storm. *Mon. Wea. Rev.*, **131**, 27–50, https://doi.org/10.1175/1520-
858   0493(2003)131<0027:OIOTMS>2.0.CO;2.

859 Ropelewski, C. F., and M. S. Halpert, 1986: North American Precipitation and Temperature
860   Patterns Associated with the El Niño/Southern Oscillation (ENSO). *Monthly Weather*
861   *Review*, **114**, 2352–2362, https://doi.org/10.1175/1520-
862   0493(1986)114<2352:NAPATP>2.0.CO;2.

863 Rowntree, P. R., 1972: The influence of tropical east Pacific Ocean temperatures on the
864   atmosphere. *Quarterly Journal of the Royal Meteorological Society*, **98**, 290–321,
865   https://doi.org/10.1002/qj.49709841605.

866 Rutz, J. J., and W. J. Steenburgh, 2012: Quantifying the role of atmospheric rivers in the
867   interior western United States. *Atmos. Sci. Lett.*, **13**, 257–261,
868   https://doi.org/10.1002/asl.392.

——, ——, and F. M. Ralph, 2014: Climatological Characteristics of Atmospheric Rivers and Their Inland Penetration over the Western United States. *Mon. Wea. Rev.*, **142**, 905–921, https://doi.org/10.1175/MWR-D-13-00168.1.

——, ——, and ——, 2015: The Inland Penetration of Atmospheric Rivers over Western North America: A Lagrangian Analysis. *Mon. Wea. Rev.*, **143**, 1924–1944, https://doi.org/10.1175/MWR-D-14-00288.1.

Ryoo, J.-M., and Coauthors, 2020: Terrain Trapped Airflows and Precipitation Variability during an Atmospheric River Event. *J. Hydrometeor.*, **21**, 355–375, https://doi.org/10.1175/JHM-D-19-0040.1.

Schaerer, P., 1989: The Avalanche-Hazard Index. *Annals of Glaciology*, **13**, 241–247, https://doi.org/10.3189/S0260305500007977.

Schweizer, J., J. Bruce Jamieson, and M. Schneebeli, 2003: Snow avalanche formation. *Rev. Geophys.*, **41**, https://doi.org/10.1029/2002RG000123.

——, C. Mitterer, and L. Stoffel, 2009: On forecasting large and infrequent snow avalanches. *Cold Reg. Sci. Technol.*, **59**, 234–241, https://doi.org/10.1016/j.coldregions.2009.01.006.

Shafer, J. C., and W. J. Steenburgh, 2008: Climatology of Strong Intermountain Cold Fronts. *Mon. Wea. Rev.*, **136**, 784–807, https://doi.org/10.1175/2007MWR2136.1.

Sinclair, M. R., 1993: A Diagnostic Study of the Extratropical Precipitation Resulting from Tropical Cyclone Bola. *Mon. Wea. Rev.*, **121**, 2690–2707, https://doi.org/10.1175/1520-0493(1993)121<2690:ADSOTE>2.0.CO;2.

Smith, R. B., Q. Jiang, M. G. Fearon, P. Tabary, M. Dorninger, J. D. Doyle, and R. Benoit, 2003: Orographic precipitation and air mass transformation: An Alpine example. *Quart. J. Roy. Meteor. Soc.*, **129**, 433–454, https://doi.org/10.1256/qj.01.212.

Smith, R. B., P. Schafer, D. Kirshbaum, and E. Regina, 2009: Orographic Enhancement of Precipitation inside Hurricane Dean. *J. Hydrometeor.*, **10**, 820–831, https://doi.org/10.1175/2008JHM1057.1.

Steenburgh, J., 2023: *Secrets of the Greatest Snow on Earth*. 2nd ed. Utah State University Press,.

Steenburgh, W. J., 2003: One Hundred Inches in One Hundred Hours: Evolution of a Wasatch Mountain Winter Storm Cycle. *Wea. Forecasting*, **18**, 1018–1036, https://doi.org/10.1175/1520-0434(2003)018<1018:OHIIOH>2.0.CO;2.

——, and S. Nakai, 2020: Perspectives on Sea- and Lake-Effect Precipitation from Japan's "Gosetsu Chitai." *Bull. Amer. Meteor. Soc.*, **101**, E58–E72, https://doi.org/10.1175/BAMS-D-18-0335.1.

——, S. F. Halvorson, and D. J. Onton, 2000: Climatology of Lake-Effect Snowstorms of the Great Salt Lake. *Mon. Wea. Rev.*, **128**, 709–727, https://doi.org/10.1175/1520-0493(2000)128<0709:COLESO>2.0.CO;2.

Stoelinga, M. T., R. E. Stewart, G. Thompson, and J. M. Thériault, 2013: Microphysical Processes Within Winter Orographic Cloud and Precipitation Systems. *Mountain Weather Research and Forecasting: Recent Progress and Current Challenges*, F.K. Chow, S.F.J. De Wekker, and B.J. Snyder, Eds., *Springer Atmospheric Sciences*, Springer Netherlands, 345–408.

Stohl, A., C. Forster, and H. Sodemann, 2008: Remote sources of water vapor forming precipitation on the Norwegian west coast at 60°N–a tale of hurricanes and an atmospheric river. *J. Geophys. Res.: Atm.*, **113**, https://doi.org/10.1029/2007JD009006.

Sturdevant-Rees, P., J. A. Smith, J. Morrison, and M. L. Baeck, 2001: Tropical storms and the flood hydrology of the central Appalachians. *Water Resour. Res.*, **37**, 2143–2168, https://doi.org/10.1029/2000WR900310.

Sui, C.-H., X. Li, and M.-J. Yang, 2007: On the Definition of Precipitation Efficiency. *J. Atmos. Sci.*, **64**, 4506–4513, https://doi.org/10.1175/2007JAS2332.1.

Trenberth, K. E., G. W. Branstator, D. Karoly, A. Kumar, N.-C. Lau, and C. Ropelewski, 1998: Progress during TOGA in understanding and modeling global teleconnections associated with tropical sea surface temperatures. *Journal of Geophysical Research: Oceans*, **103**, 14291–14324, https://doi.org/10.1029/97JC01444.

Valenzuela, R. A., and D. E. Kingsmill, 2015: Orographic Precipitation Forcing along the Coast of Northern California during a Landfalling Winter Storm. *Mon. Wea. Rev.*, **143**, 3570–3590, https://doi.org/10.1175/MWR-D-14-00365.1.

——, and ——, 2017: Terrain-Trapped Airflows and Orographic Rainfall along the Coast of Northern California. Part I: Kinematic Characterization Using a Wind Profiling Radar. *Mon. Wea. Rev.*, **145**, 2993–3008, https://doi.org/10.1175/MWR-D-16-0484.1.

Veals, P. G., W. J. Steenburgh, S. Nakai, and S. Yamaguchi, 2020: Intrastorm Variability of the Inland and Orographic Enhancement of a Sea-Effect Snowstorm in the Hokuriku Region of Japan. *Mon. Wea. Rev.*, **148**, 2527–2548, https://doi.org/10.1175/MWR-D-19-0390.1.

Viale, M., and M. N. Nuñez, 2011: Climatology of Winter Orographic Precipitation over the Subtropical Central Andes and Associated Synoptic and Regional Characteristics. *J. Hydrometeor.*, **12**, 481–507, https://doi.org/10.1175/2010JHM1284.1.

Wasserstein, M. L., and W. J. Steenburgh, 2023: Alta-Collins Snow and Liquid Precipitation Equivalent Observations 2000–2023, accessed 1 September 2023, https://toi.lib.utah.edu/resolve/10.7278/S50d-nsy5-8bje

Whiteman, C. D., 2000: Mountain Climates of North America. *Mountain Meteorology: Fundamentals and Applications*, C.D. Whiteman, Ed., Oxford University Press, p. 0.

Whittaker, L. M., and L. H. Horn, 1981: Geographical and Seasonal Distribution of North American Cyclogenesis, 1958–1977. *Mon. Wea. Rev.*, **109**, 2312–2322, https://doi.org/10.1175/1520-0493(1981)109<2312:GASDON>2.0.CO;2.

950 Williams, P., and E. L. Peck, 1962: Terrain Influences on Precipitation in the Intermountain
951   West as Related to Synoptic Situations. *J. Appl. Meteor. Climatol.*, **1**, 343–347,
952   https://doi.org/10.1175/1520-0450(1962)001<0343:TIOPIT>2.0.CO;2.

953 Wolter, K., and M. S. Timlin, 2011: El Niño/Southern Oscillation behaviour since 1871 as
954   diagnosed in an extended multivariate ENSO index (MEI.ext). *International Journal*
955   *of Climatology*, **31**, 1074–1087, https://doi.org/10.1002/joc.2336.

956 Wood, V. T., R. A. Brown, and S. V. Vasiloff, 2003: Improved Detection Using Negative
957   Elevation Angles for Mountaintop WSR-88Ds. Part II: Simulations of the Three
958   Radars Covering Utah. *Wea. Forecasting*, 18, 393–403, https://doi.org/10.1175/1520-
959   0434(2003)18<393:IDUNEA>2.0.CO;2.

960 Wulfmeyer, V., and Coauthors, 2011: The Convective and Orographically-induced
961   Precipitation Study (COPS): the scientific strategy, the field phase, and research
962   highlights. *Quart. J. Roy. Meteor. Soc.*, **137**, 3–30, https://doi.org/10.1002/qj.752.

963 Yeager, K. N., W. J. Steenburgh, and T. I. Alcott, 2013: Contributions of Lake-Effect Periods
964   to the Cool-Season Hydroclimate of the Great Salt Lake Basin. *J. Appl. Meteor.*
965   *Climatol.*, **52**, 341–362, https://doi.org/10.1175/JAMC-D-12-077.1.

966 Yuter, S. E., D. A. Stark, J. A. Crouch, M. J. Payne, and B. A. Colle, 2011: The Impact of
967   Varying Environmental Conditions on the Spatial and Temporal Patterns of
968   Orographic Precipitation over the Pacific Northwest near Portland, Oregon. *J.*
969   *Hydrometeor.*, **12**, 329–351, https://doi.org/10.1175/2010JHM1239.1.

970 Zishka, K. M., and P. J. Smith, 1980: The Climatology of Cyclones and Anticyclones over
971   North America and Surrounding Ocean Environs for January and July, 1950–77. *Mon.*
972   *Wea. Rev.*, **108**, 387–401, https://doi.org/10.1175/1520-
973   0493(1980)108<0387:TCOCAA>2.0.CO;2.

974